https://doi.org/10.5194/essd-2025-551
Preprint. Discussion started: 13 March 2026

Open Access Earth System Science Data Discussions

Mercury dataset over the Third Pole

Shichang Kang [1,2,8]*, Jie Huang [1,8]*, Qianggong Zhang [3,8], Junming Guo [1], Xiufeng Yin [1], Shiwei Sun [1], Xuejun Sun [4], Lekhendra Tripathee [5], Sabur Abdullaev [6], Wenjun Tang [3], Yi Zhang [3,8], Xiwen Miao [1,7], Liujian Liao [1,8], Lusheng Che [1,8]

[1] *State Key Laboratory of Cryospheric Science and Frozen Soil Engineering, Northwest Institute of Eco-Environment and Resources, Chinese Academy of Sciences, Lanzhou 730000, China*
[2] *Institute of Mountain Hazards and Environment, Chinese Academy of Sciences, Chengdu 610213, China*
[3] *State Key Laboratory of Tibetan Plateau Earth System, Environment and Resources, Institute of Tibetan Plateau Research, Chinese Academy of Sciences, Beijing 100101, China*
[4] *School of Environmental and Resource Sciences, Shanxi University, Taiyuan 030006, China*
[5] *Environment Agency, Newcastle NE4 7AR, United Kingdom*
[6] *Physical Technical Institute of the Academy of Sciences of Tajikistan, Dushanbe 734063, Tajikistan*
[7] *Key Laboratory of Western China's Environmental Systems (Ministry of Education), College of Earth and Environmental Sciences, Lanzhou University, Lanzhou 730000, China*
[8] *University of Chinese Academy of Sciences, Beijing 100049, China*

Correspondence to: Profs. Shichang Kang (shichang.kang@lzb.ac.cn) & Jie Huang (jiehuang@nieer.ac.cn)

Abstract

The Tibetan Plateau and its surrounding regions, collectively known as the Third Pole, constitute one of Earth's largest topographic and cryospheric features, playing a pivotal role in the cycling of trace elements at both regional and global scales. Mercury (Hg), a toxic heavy metal of global concern, has garnered increasing attention due to its detrimental effects on environmental and human health. Large-scale atmospheric circulation facilitates the long-range transport of atmospheric Hg pollutants, which can subsequently be deposited across the Third Pole. Over recent decades, the Atmospheric Pollution and Cryospheric Change (APCC) program has established and sustained an integrated monitoring network throughout this region to systematically examine the interactions between Hg biogeochemical cycling and cryospheric changes. This paper presents a comprehensive Hg dataset encompassing air (2 stations), aerosols (9 stations), precipitation (16 stations), glaciers (12 glaciers; including snowpit, surface snow, and cryoconite samples), soils (50 sites), surface waters (53 locations; including river, lake, and glacial meltwater), glacier ice cores (1 core), and lake sediment cores (8 cores) collected across the Third Pole. The data were acquired through both in situ (online) monitoring and laboratory analyses. High-resolution atmospheric Hg concentrations were measured using a Tekran 2537B analyzer at the Nam Co and Tanggula stations. Spatial and temporal distributions of Hg in aerosols, precipitation, glaciers, soils, and sediment cores revealed distinct patterns and trends across different sectors of the Third Pole, influenced significantly by emission sources, transport pathways, and

https://doi.org/10.5194/essd-2025-551
Preprint. Discussion started: 13 March 2026

Open Access Earth System Science Data Discussions

environmental processes. Depositional chronologies derived from glacier ice and lake sediment cores reflect anthropogenic perturbations in the historical Hg record since the Industrial Revolution. Stable Hg isotope compositions from aerosols, soils, and lake sediments provide evidence for transboundary transport of Hg pollution and its northward incursion into the interior Tibetan Plateau from South Asia. This updated dataset is made publicly available to support interdisciplinary research linking the cryosphere, atmosphere, soils, and hydrology. The data are archived in standardized Excel format and accessible through the institutional repository of the State Key Laboratory of Cryospheric Science and Frozen Soil Engineering, Northwest Institute of Eco-Environment and Resources, Chinese Academy of Sciences, Lanzhou (*Kang et al., 2024*).

Keywords

Mercury, Air, Aerosol, Precipitation, Glacier, Soil, Surface water, Glacier ice core, Lake sediment cores, Isotope signature, The Third Pole

Abbreviations

TSP Total Suspended Particulates
TGM Total Gaseous Mercury
ISM Indian Summer Monsoon
Hg_T Total Hg
Hg_P Particulate-bound Hg
Hg_D Dissolved Hg
Hg_R Reactive Hg
MeHg Methyl Hg

1. Introduction

The Tibetan Plateau and its surrounding regions, referred to as the Third Pole, form the highest and most extensive plateau on Earth, with an average elevation exceeding 4000 m a.s.l. and an area of approximately 2.5 million km². Known as the “Asian Water Tower” (Immerzeel et al., 2010; Yao et al., 2022), this hydrologically critical region acts as the headwater source for many major Asian rivers, supplying freshwater to billions of people downstream. Owing to its vast and complex topography, the Third Pole significantly influences climate systems, cryospheric changes, environmental processes, and biogeochemical cycles at both regional and global scales. It has experienced accelerated warming at a rate of 0.34 °C decade^{-1} (You et al., 2021), surpassing the Northern Hemisphere average (0.29 °C decade^{-1}) and global trends (Kang et al., 2010; Chen et al., 2015). This pronounced warming drives rapid cryospheric loss, including glacier retreat, permafrost degradation, and decline in snow cover (Yao et al., 2019), profoundly impacting Earth system dynamics across the Third Pole.

Mercury (Hg) is a globally prioritized pollutant owing to its high toxicity, bioavailability, and capacity for trophic magnification in aquatic ecosystems (Kim et al., 2016). Methyl Hg (MeHg), one of the most concerning organic Hg species (Mergler et al., 2007), bioaccumulates in aquatic food webs and biomagnifies across trophic levels, posing substantial neurotoxic threats to human health (Grandjean et

https://doi.org/10.5194/essd-2025-551
Preprint. Discussion started: 13 March 2026

al., 2010; Beckers and Rinklebe, 2017). Recognized as a critically problematic contaminant (Driscoll et al., 2013), Hg became regulated under international policy through the adoption of the Minamata Convention in 2013 (Kessler, 2013; Selin et al., 2018).

Under rapid warming conditions, environmental transformations across the Third Pole may exhibit distinctive features in Hg biogeochemical cycling (Kang et al., 2019; Sun et al., 2020a). However, the remote and expansive nature of the region-coupled with complex topography, limited accessibility, extreme climate, and harsh environmental conditions-poses considerable challenges for Hg investigation across various compartments. Although regional and global chemical transport models (e.g., GEOS-Chem, CMAQ-Hg) have provided valuable insights into Hg dynamics (Lin et al., 2010; Wang et al., 2014), observational data remain essential for validating and refining atmospheric transport models in this data-scarce region. Furthermore, while models excel at simulating spatial patterns of Hg over broad scales, they often lack the temporal resolution needed to capture rapid changes and underlying transformation mechanisms-gaps that high-resolution Hg measurements can help address. The current scarcity of Hg data underscores the urgent need for enhanced observational efforts across the Third Pole.

In recent decades, our research team has established the Atmospheric Pollution and Cryospheric Changes (APCC) program-an integrated monitoring network and research initiative focused on interactions between atmospheric pollution and cryospheric environments across the Third Pole (Kang et al., 2019). Building on the APCC framework, recent advances in observational instrumentation and techniques have been employed to characterize environmental Hg processes, including its spatial and temporal distributions, transport pathways, and deposition mechanisms in this region. A series of observational findings linked to the APCC program have been consistently published. Consequently, research on Hg across various environmental compartments of the Third Pole has achieved substantial scientific progress over the past decades. In this paper, we provide a concise overview of our previous studies and present an organized compilation of systematic Hg datasets derived from air, aerosols, precipitation, glaciers, soils, surface water (river, lake, and glacial meltwater), glacier ice and lake sediment core across the Third Pole.

The paper is structured as follows: Sections 2 and 3 outline the descriptions of observation sites, field sampling procedures, and measurement methodologies; Section 4 provides a comprehensive presentation of Hg datasets from air, aerosols, precipitation, glaciers, soils, surface water, glacier ice, and lake sediment cores, along with a detailed description of Hg stable isotope compositions in aerosols, soils, and lake sediments; Section 5 addresses data accessibility; and Section 6 presents the concluding remarks.

2. Observation site descriptions

2.1 Overview of site distributions

The Third Pole comprises the Himalayas and Tibetan Plateau (hereafter Himalaya-Tibet), along with surrounding areas including China's Xinjiang Uyghur Autonomous Region and parts of South Asia (e.g., Nepal, India) and Central Asia (e.g., Kazakhstan, Tajikistan) (Fig. 1). Topographically, it is characterized by the high-altitude Himalaya-Tibet region (mean elevation >4,000 m a.s.l.) in the south

https://doi.org/10.5194/essd-2025-551
Preprint. Discussion started: 13 March 2026

and extensive arid basins (e.g., Tarim, Qaidam) in the northwest. The region is divided into two atmospheric regimes: a northern domain dominated by westerlies (winter) and a southern domain influenced by monsoons (summer), driven by seasonal circulation shifts (Fig. 1).

Under the APCC program, multi-compartment Hg observations were conducted across dozens of stations (Fig. 1; Table 1), including:2 stations for online air monitoring, 9 stations for aerosol sampling, 16 stations for precipitation collection, 12 glaciers for snowpit, surface snow, and cryoconite sampling, 50 sites for soil sampling, and 53 locations for surface water sampling. Sampling elevations ranged from 13 m to 6,000 m a.s.l., covering diverse landscapes (e.g., forest, grassland, glacier, river, lake, frozen ground, and desert). Additionally, one alpine ice core and eight lake sediment cores were obtained to reconstruct historical Hg deposition (Fig. 1; Tables 2, 3). This study releases a comprehensive Hg dataset from these environmental matrices (APCC datasets I-1 to I-8). All sampling details-location, elevation, and sample type-are provided in Table 1 and illustrated in Fig. 1. Sites are described in the following sections by environmental category.

2.2 Air sites

Total gaseous Hg (TGM) concentrations were monitored at two inland Tibetan Plateau stations: Nam Co Station (30°46.44′N, 90°59.31′E; 4,730 m a.s.l.) and Tanggula Station (33°00′35″N, 91°58′28″E; 5,050 m a.s.l.) (APCC dataset I-1; Yin et al., 2018; Sun et al., 2020b). Both sites experience minimal local anthropogenic influence. Land-air Hg exchange fluxes were additionally quantified at Tanggula Station (Sun et al., 2020b).

The Nam Co Station, located between Nam Co Lake and the Nyainqêntanglha mountain range, is characterized by minimal local anthropogenic Hg emission sources (Fig. 1). Situated in continuous permafrost with alpine grassland landscapes, Tanggula Station lies near the northern limit of Indian summer monsoon (ISM) intrusion (Fig. 1). Atmospheric circulation shifts seasonally between ISM (warm months) and mid-latitude westerlies (cold seasons) (Tian et al., 2007; Yao et al., 2013). The nearest settlements-Yanshiping (65 km north) and Anduo (110 km south)-are distant, with nomadic grazing as the primary human activity. This station provides an ideal setting for studying atmospheric Hg dynamics, including long-range transport and land-air exchange processes, in the remote central Tibetan Plateau (Sun et al., 2020b).

2.3 Aerosol sites

Aerosol Hg sampling was conducted at 10 sites across the Third Pole (Fig. 1; APCC dataset I-2). Three stations-Kathmandu, Dhulikhel (DHK), and Lumbini (LMB)-are located on the southern Himalayan slope in Nepal, capturing Hg emissions from urban, agricultural, and industrial sources to trace transboundary pollution transport (Guo et al., 2017, 2021, 2022). Kathmandu (Bode (BD) and DHK sites) represents a rapidly urbanizing area with severe air pollution; LMB, a UNESCO World Heritage site situated in the Indo-Gangetic Plains, reflects mixed agricultural and industrial influences.

On the Tibetan Plateau, aerosol Hg was measured at Lhasa Station (LS) (Fig. 1), the region's largest city, where economic growth has intensified local Hg pollution through urbanization and industrial expansion (Huang et al., 2016). Five additional stations were established in the Taklimakan

https://doi.org/10.5194/essd-2025-551
Preprint. Discussion started: 13 March 2026

Desert (Fig. 1)-Kashgar (KS), Taxkorgan (TX), Minfeng (MF), Ruoqiang (RQ), and Tazhong (TZ)-to monitor dust-associated Hg in this major Northern Hemisphere dust source (APCC dataset I-2; Huang et al., 4).

2.4 Precipitation sites

Precipitation Hg was measured at 12 stations across the Third Pole (APCC dataset I-3; Huang et al., 2022, 2024), comprising 6 stations in the monsoon domain (Nam Co (NMC), Southeast Tibet (SET), Mt. Everest (EV), Yulong (YL) and Motuo (MT)) and 6 in the westerlies domain (Akedala (AK), Tianshan (TS), Muztagh Ata (MZ), Laohugou (LHG) and Ngari (NA)) (Fig. 1; Table 1). Both regions show strong seasonal precipitation concentration, with ~80% (monsoon) and ~86% (westerlies) occurring in summer due to moisture transport from the Indian Ocean and North Atlantic, respectively, and minimal rainfall from October to April (Huang et al., 2022).

On the southern Himalayan slopes, five precipitation Hg sampling sites were established in Nepal (APCC dataset I-3; Table 1), spanning urban to remote alpine environments: Kathmandu (1,314 m a.s.l.), Dhunche (DC) (2,065 m a.s.l.), Jomsom (JMS) (2,750 m a.s.l.), Dimsa (DM) (3,078 m a.s.l.), and Gosainkunda (GSK) (4,417 m a.s.l.) (Tripathee et al., 2019, 2020). These sites represent varied settings-urban, rural, forested, and high-altitude remote areas-along key geographic and trekking corridors in the central Himalayas.

2.5 Glacier sites

Hg distribution across glaciers in the Third Pole was systematically documented using a dataset from 12 glaciers (Zhang et al., 2012; APCC dataset I-4), selected to represent diverse climatic and geographic settings. Sampling elevations ranged from ~3,600 m a.s.l. (Muz Taw Glacier, northern Xinjiang) to ~6,500 m a.s.l. (East Rongbuk Glacier, Mt. Everest) (Tables 1 and 2), providing a pronounced spatial and temporal gradients for examining Hg variability.

Five glaciers are located within the monsoon domain (Fig. 1 and Table 2): Baishui No.1 (Mt. Yulong), Demula and Yarlong No.4 (southeastern Tibetan Plateau), East Rongbuk (central Himalayas), and Zhadang (western Nyainqentanglha Mts.). Seven glaciers fall within the westerlies domain (Fig. 1 and Table 2): Xiao Dongkemadi (headwaters of the Yangtze River), Ganglongjiama (Mt. Geladaindong, Tanggula Mts.), Laohugou No.12 (Qilian Mts.), Shiyi (Yeniugou basin, Qilian Mts.), Muztag Ata (Pamir Plateau), Urumqi No.1 (headwaters of Urumqi River, eastern Tianshan), and Muz Taw (Sawir Mts., northern Xinjiang).

2.6 Soil sites

The Third Pole contains the most extensive low- and mid-latitude permafrost on Earth, accounting for 74.5% of Northern Hemisphere high-mountain permafrost (Yang et al., 2010). A total of 31 surface frozen soil samples (5 ± 0.5 cm depth) were collected from permafrost sites >3,000 m a.s.l. along this transect, including 21 sites on the southern Himalayan slope and 10 on the northern slope (Huang et al., 2020b; APCC dataset I-5).

Climatic, topographic, and biological gradients support diverse vegetation types including forests,

https://doi.org/10.5194/essd-2025-551
Preprint. Discussion started: 13 March 2026

steppes, meadows, grasslands, and shrublands (Yin et al., 2024). A total of 336 soil samples were collected from 28 sites (meadow: n = 5; grassland: n = 7; desert: n = 10; forest: n = 6) across the Tibetan Plateau (2,917-4,762 m a.s.l.). An additional 36 soil samples were obtained from Langtang National Park (28.15-28.21°N, 85.39-85.56°E) in the Nepal Himalayas.

Topsoil samples (0-5 cm) were also collected from arid regions of Central Asia (Tajikistan, Uzbekistan, Kyrgyzstan; Figs. 1 and 6), covering 2.45×10^6 km². These 182 samples (Yang et al., 2023; APCC dataset I-5) enable comparative analysis of soil Hg across different arid landscapes and assessment of anthropogenic impacts in Central Asia.

2.7 Surface water sites

Surface water Hg datasets (APCC dataset I-6) across the Third Pole include 2 rivers (Zheng et al., 2010; Sun et al., 2020c), 42 lakes (Li et al., 2015), and 9 glacier-fed streams (Sun et al., 2016, 2017, 2022; Paudyal et al., 2017, 2019; Pu et al., 2024; Wang et al., 2024). The rivers comprise the Yarlung Zangbo (Brahmaputra upstream), a high-altitude (>4,000 m a.s.l.) system originating from the Jiemayangzong Glacier (30°48'N, 82°42'E) and draining 239,228 km² across southern Tibet, and the transboundary Koshi River, which flows through China (33% of its 87,311 km² basin), Nepal (45%), and India (22%).

Lake waters were sampled from 42 endorheic lakes (APCC dataset I-6) spanning altitudes of 3,469-5,145 m a.s.l. and surface areas from <1 km² to >1,000 km², providing broad geographic and limnological coverage of Hg distribution patterns (Li et al., 2015).

Glacial meltwater sampling covered 9 glacier runoffs (APCC dataset I-6) representing key regions: Laohugou No.12 (Qilian Mts.), Xiao Dongkemadi (Tanggula Mts.), Zhadang and Kuoqionggangri (Nyainqentanglha Mts.), Qiangyong and Rongbuk (Himalayas), and Hailuogou (Mt. Gongga), Baishuihe No.1 (Mt. Yulong), and Mingyong (Mt. Meili) on the southeastern Tibetan Plateau.

2.8 Glacier ice and sediment cores sites

A 147 m ice core was retrieved in 2005 from Ganglongjiama Glacier (33.58°N, 91.18°E; 5,750 m a.s.l.) on Mt. Geladaindong (6,621 m a.s.l.), which is the headwaters of the Yangtze River and the highest peak in the Tanglha Range, central Tibetan Plateau (Kang et al., 2016; APCC dataset I-7; Fig. 1).

Eight profundal sediment cores were collected between 2008 and 2011 using a 6-cm diameter gravity corer from Himalayan (Phewa, Gokyo, Gosainkunda) and Tibetan (Qiangyong Co, Nam Co, Bangong Co, Lingge Co, Tanglha) lakes (APCC dataset I-7; Fig. 1; Table 3). These lakes represent key environmental gradients: Phewa Lake (28.21°N, 83.95°E; 782 m a.s.l.; 4.35 km²; 22.5 m depth) receives urban/agricultural runoff in the Pokhara Valley; Gosainkunda Lake (28.08°N, 85.42°E; 4,300 m a.s.l.; 0.14 km²; 24.1 m depth) is an oligotrophic system in Langtang National Park; Gokyo Lake (27°58'N, 86°40'E; 4,700-5,000 m a.s.l.) is an ultra-oligotrophic system near Mt. Everest. The five Tibetan lakes span southern (Qiangyong Co), southwestern (Bangong Co), and inland (Nam Co, Lingge Co, Tanglha) regions (Fig. 1).

3. Field sampling and measurement methods

https://doi.org/10.5194/essd-2025-551
Preprint. Discussion started: 13 March 2026

3.1 Air

Atmospheric TGM was monitored at Nam Co Station (2012-2014) using a Tekran 2537B analyser (Tekran Instruments Corp., Canada). Air was sampled through a rooftop inlet equipped with a 0.2 μm Teflon filter, replaced biweekly. The instrument employed dual gold cartridges for continuous Hg collection, thermal desorption, and detection by CVAFS at 253.7 nm. Sampling interval was 5 min at 0.8 L min^{-1}. Calibration was performed automatically every 25 h and manually annually using a Tekran 2505 unit. TGM at this site consisted predominantly (>98%) of gaseous elemental Hg (GEM) (Yin et al., 2018; de Foy et al., 2016).

At Tanggula Station, TGM was measured similarly with a ground-level inlet ~1 m above the surface (Sun et al., 2020b). Land-air Hg fluxes were quantified using a dynamic flux chamber (DFC) coupled to a Tekran 2537B, alternating between ambient and chamber air every 5 min at 1.5 L min^{-1}. Hg fluxes were calculated from the TGM difference, normalized to flow rate and chamber area. A 0.2 μm Teflon filter was used to remove Hg_P from sampled air. Quality assurance showed system blanks of 0.00 ± 0.01 ng m^{-3} in 95% of measurements. Manual injections indicated an accuracy of ~96% and precision <3%. Flux blanks averaged 0.002 ± 0.010 ng m^{-2} h^{-1}, demonstrating negligible systematic bias (Sun et al., 2020b).

3.2 Aerosol

Total Suspended Particles (TSP) were collected on pre-combusted quartz fiber filters (Whatman® GF/F; 90 mm, 2.2 μm pore size) using high-volume samplers (KC-120H or RP 1400a) operated at 100 L min^{-1}. Sampling durations were 24 h at urban/rural sites and 48 h at remote sites. Samplers were mounted on building rooftops to minimize ground interference. Filters were equilibrated (>24 h, 25 °C, 30% RH) before and after sampling for gravimetric analysis. Collected samples were sealed and stored at 4 °C until analysis.

Aerosol Hg concentrations were measured in duplicate using a Leeman Hydra II_C Direct Hg Analyzer (Teledyne Leeman Labs, Hudson, New Hampshire, USA). A 0.5 cm^2 filter aliquot was thermally decomposed, amalgamated, and quantified by cold vapor atomic absorption spectroscopy (CVAAS) following US EPA Method 7473. Quartz filters were selected for their low Hg blanks, thermal stability, and suitable airflow properties (Huang et al., 2016; Guo et al., 2017, 2021).

3.3 Precipitation

Precipitation samples were collected using an automated wet deposition sampler (SYC-2, Laoshan Electronic Instrument Complex Co., Ltd.). After 24-hour collection in HDPE bags, samples were partitioned for analysis of total Hg (Hg_T), dissolved Hg (Hg_D), and MeHg. Aliquots for Hg_T were transferred to 50-mL polypropylene BD Falcon® centrifuge tubes, and for MeHg to acid-cleaned 50-mL borosilicate glass bottles; both were preserved with HCl to 0.5% (v:v). Samples exceeding 50 mL were filtered within 24 h using a borosilicate filtration system with 0.45-μm pore size and 47-mm diameter Durapore membranes (Millipore). Filtered samples were collected in polypropylene tubes and acidified for Hg_D analysis. Hg_P was calculated as Hg_T–Hg_D. Field blanks were prepared using ultra-pure water exposed during sampling. All samples were stored at 4 °C under strict contamination control protocols

https://doi.org/10.5194/essd-2025-551
Preprint. Discussion started: 13 March 2026

(Huang et al., 2013, 2022).

Hg_T and Hg_D were analyzed following US EPA Method 1631 (rev. E) via BrCl oxidation, $NH_2OH{\cdot}HCl$ quenching, $SnCl_2$ reduction, and detection by CVAFS in an ultra-clean laboratory (Class 100-1000). MeHg was determined by aqueous distillation, ethylation with $NaBEt_4$, purge and trap on Tenax, and analysis by gas chromatography (GC)-CVAFS. The method detection limit for MeHg was 0.01 ng L^{-1} (Huang et al., 2012a). All procedures were conducted in a metal-free environment to prevent contamination.

3.4 Glacier

Snowpit sampling was conducted to determine the vertical variations of Hg in glaciers (Zhang et al., 2012; Huang et al., 2014b). Pits were excavated to 1-2 m depth, and duplicate or quadruplicate samples were collected from each layer to ensure representativeness. Samples were placed in pre-cleaned Whirl-Pak bags, sealed immediately, and stored in insulated coolers to maintain frozen conditions during transport. Field blanks and duplicates were used for quality control. Samples were stored at -20 °C until analysis. Hg concentrations were measured following US EPA Method 1631, as applied to precipitation samples (Section 3.3), after melting at room temperature in a clean lab (Huang et al., 2012b; Zhang et al., 2012).

Surface snow and cryoconite samples were collected to assess the spatial and altitudinal distribution of Hg across the Tibetan Plateau (Huang et al., 2012b, 2019). Surface snow was sampled in triplicate at 5 cm intervals using acid-washed polystyrene scoops under a “clean hands-dirty hands” protocol with non-powder gloves and protective clothing. Cryoconite granules (solid-phase, <5% ice) were collected with pre-cleaned stainless steel tools, stored in amber glass bottles, and kept frozen throughout. Tools were rinsed with 0.1% HCl and ultrapure water between samples to avoid cross-contamination.

Hg concentrations in surface snow were determined using US EPA Method 1631, consistent with the methodology applied to snowpit samples. Cryoconite samples were freeze-dried, and Hg_T was analyzed using a Leeman Hydra-II_C Hg analyzer (Huang et al., 2019). Approximately 0.2 g of sample was used per measurement. The method detection limit (MDL) was 0.06 ng g^{-1}, reproducibility (RPD) was <5%, and recoveries for certified reference material GSS-9 ranged from 98% to 103%.

3.5 Soil

During topsoil sampling, Global Positioning System (GPS) coordinates and land cover type were documented at each site. Surface debris was cleared prior to collecting the 0-5 cm layer with a stainless-steel shovel. Samples were sealed in labeled polyethylene bags and stored in insulated containers (Yang et al., 2023). For soil pit sampling, three replicate pits were excavated within a 1 m × 1 m area (Yin et al., 2024). Samples were taken at 0-10 cm, 10-20 cm, 20-30 cm, and 30-40 cm depths from a 20 cm × 20 cm face, placed in pre-labeled ziplock bags, and transported to the laboratory for frozen storage.

Freeze-dried soil samples were ground with a quartz mortar and sieved to <150 μm. Hg_T was analyzed in duplicate using a Leeman Hydra II_C Hg analyzer via thermal decomposition, amalgamation, and CVAAS detection, following US EPA Method 7473. Approximately 0.2 g of sample was used per

https://doi.org/10.5194/essd-2025-551
Preprint. Discussion started: 13 March 2026

measurement. Calibration was performed with $HgCl_2$ standard solutions, yielding linear response ($r^2 > 0.999$). Quality assurance included analysis of certificated reference materials GSS-9 and Tort-2 every 10 samples, with recoveries ranging from 95% to 105%. The method detection limit (MDL) was <0.02 ng g^{-1}, and replicate precision was <5% RSD (Yang et al., 2023). The same analytical procedures were applied as for aerosol and cryoconite samples.

3.6 Surface water

Surface water samples were collected in duplicate using pre-cleaned 50 mL centrifuge tubes or 250 mL FLPE bottles (Nalgene®). All containers were pre-tested for blanks and adsorption, meeting field sampling requirements. Samples were obtained using a "Clean Hands-Dirty Hands" protocol with polyethylene gloves to prevent contamination. Prior to sampling, each bottle was rinsed 3 times with ambient water. Samples were taken with the bottle opening facing upstream to collect surface water without disturbing bottom sediments. Field blanks, prepared using ultrapure water in pre-cleaned polypropylene tubes, were included at a rate of 10%.

Within 24 hours of collection, water samples were filtered through Millipore membranes (0.45 μm and 47-mm). The filtration apparatus was rinsed 3 times with ultrapure water before and after each sample to avoid cross-contamination. Both Hg_T and Hg_D were preserved on-site by acidification to 0.5% (v/v) with MOS-grade HCl to minimize adsorption and transformation. Samples were transported refrigerated and stored at 4 °C until analysis.

Hg_T and Hg_D were analyzed following US EPA Method 1631, as applied to precipitation and snow samples (Sections 3.3, 3.4). Samples were oxidized with 50 μL BrCl, followed by quenching with $NH_2OH{\cdot}HCl$ and reduction with $SnCl_2$; Hg^0 was quantified by CVAFS. Hg_P was calculated as the difference between Hg_T and Hg_D.

3.7 Glacier ice core and lake sediment cores

The ice core was maintained at <-15°C during transport and storage. In a cold laboratory, it was sectioned into 5-10 cm segments using a bandsaw. Each segment was decontaminated with a ceramic knife to remove outer layers and subsequently melted at room temperature in a Class-100 metal-free clean lab (Kang et al., 2016), yielding >30 mL of meltwater for Hg analysis. Hg concentrations are reported in ng L^{-1} and were determined following the same analytical protocols applied to precipitation, snow, and water samples (Sections 3.3, 3.4, 3.6).

Sediment cores were sub-sectioned at 0.5-1 cm intervals with a stainless steel slicer, stored in pre-cleaned polyethylene bags, and kept frozen until analysis. Freeze-dried and homogenized sediment aliquots (~0.2 g dry weight) were used for both Hg analysis and complementary radiometric dating (Kang et al., 2016). Hg concentrations in sediments were analyzed using the same Hg analyzer as for aerosol, cryoconite, and soil samples (Sections 3.2, 3.4, 3.5), in accordance with US EPA Method 7473.

3.8 Stable Hg isotopic composition analysis

Samples and MESS-1 reference materials (National Research Council Canada) were digested with 5 mL aqua regia (3:1 HCl:HNO_3) at 95 °C for 6 h. Digested solutions were diluted to 0.3-0.5 ng mL^{-1}

https://doi.org/10.5194/essd-2025-551
Preprint. Discussion started: 13 March 2026

Hg in a 10-20% aqua regia matrix for isotopic analysis on a Neptune Plus MC-ICP-MS. Both Hg concentration and acid matrix were matched between samples and the NIST SRM 3133 standard. Hg isotopic ratios (δ^{202}Hg, Δ^{199}Hg, Δ^{201}Hg) were reported relative to NIST SRM 3133 using standard delta notation (Bergquist and Blum, 2007).

Quality control included repeated analyses of UM-Almadén secondary standard and MESS-1. Measured values for UM-Almadén (δ^{202}Hg = -0.52 ± 0.08‰; Δ^{199}Hg = -0.01 ± 0.03‰; Δ^{200}Hg = 0.00 ± 0.02‰; Δ^{201}Hg = -0.02 ± 0.03‰) and MESS-1 (δ^{202}Hg = -1.86 ± 0.08‰; Δ^{199}Hg = 0.01 ± 0.04‰; Δ^{200}Hg = 0.01 ± 0.02‰; Δ^{201}Hg = -0.02 ± 0.04‰) agree well with published values (Yin et al., 2016a, b).

4. Data descriptions

4.1 Real-time atmospheric Hg observation

The average TGM concentration at Nam Co Station (2012-2014) was 1.33 ± 0.24 ng m^{-3} (Fig. 2), among the lowest values reported for remote areas in China (APCC dataset I-1; Yin et al., 2018). It was slightly lower than the Northern Hemisphere background but higher than Southern Hemisphere averages (Sprovieri et al., 2016). A slight decreasing trend in monthly TGM was consistent with hemispheric-scale declines in atmospheric Hg (Tong et al., 2016; Zhang et al., 2016). Seasonal variation showed a summer peak (1.50 ± 0.20 ng m^{-3}), likely due to soil re-emission and transport from South Asia (Yin et al., 2018), and a winter minimum (1.14 ± 0.18 ng m^{-3}), potentially resulting from halogen-driven removal processes (de Foy et al., 2016). Diurnal variations exhibited morning and evening peaks, accurately captured by model simulations (r^2 = 0.91-0.99; Yin et al., 2018).

At Tanggula Station, TGM exhibited a clear decreasing trend during the growing season: emergence period (2.32 ± 0.51 ng m^{-3}) > active growth (2.01 ± 0.25 ng m^{-3}) > peak vegetation (1.80 ± 0.26 ng m^{-3}) (Sun et al., 2020b; APCC dataset I-13). Higher TGM during emergence was associated with enhanced land-air Hg emissions. A subsequent increase during the ISM period coincided with strengthened westerlies (Sun et al., 2020b). Autumn TGM (2.11 ± 0.25 ng m^{-3}) reached levels similar to the emergence phase, despite lower terrestrial fluxes, suggesting limited ISM-transported Hg influence inland (Sun et al., 2020b). This pattern contrasts with summer maxima observed at southern Tibetan sites (Yin et al., 2018).

Land-air Hg fluxes decreased logarithmically during the growing season-from 3.47 ± 4.39 ng m^{-2} h^{-1} (emergence) to near zero (peak vegetation; APCC dataset I-1), primarily due to vegetation shading suppressing soil emissions. Plant uptake played a minor role given the sparse biomass (Sun et al., 2020b). Surface emissions represent a major TGM source across the remote Tibetan Plateau, where anthropogenic impacts are negligible (Sun et al., 2020b).

4.2 Hg from aerosol

Measurements of Hg_P on TSP were conducted at multiple stations across the Third Pole as part of the Atmospheric Pollution and Cryospheric Change (APCC dataset I-2). In the Taklimakan Desert, Hg_P concentrations ranged from 224.4 to 257.1 pg m^{-3}, markedly higher than those observed at typical Chinese background sites. A distinct seasonal peak occurred during frequent dust storm episodes from

https://doi.org/10.5194/essd-2025-551
Preprint. Discussion started: 13 March 2026

Open Access Earth System Science Data Discussions

March to August (Huang et al., 2020b). Preliminary emission estimates indicate that atmospheric dust originating from this region could export Hg at a rate of 59.7 ± 60.3 Mg yr^{-1} (Huang et al., 2020b).

At the high-altitude Lhasa Station, Hg_P concentrations varied widely from 61.2 to 831 pg m^{-3}, with a mean value of 224 pg m^{-3}, comparable to levels recorded in heavily polluted Chinese megacities (Huang et al., 2016). Dry deposition was identified as the dominant process in the local Hg cycle, with an estimated flux of 35.3 μg m^{-2} yr^{-1}, significantly exceeding the wet deposition flux of 8.2 μg m^{-2} yr^{-1}.

In the Kathmandu Valley, Hg_P levels were exceptionally high, averaging 850.5 ± 962.8 pg m^{-3}, which was among the highest reported for urban areas globally (Guo et al., 2017). Concentrations exhibited strong seasonality, with elevated values during winter and pre-monsoon periods. The corresponding dry deposition flux reached 135 μg m^{-2} yr^{-1}. Similarly, at LMB on the Indo-Gangetic Plains, Hg_P concentrations (range: 6.8-351.7 pg m^{-3}; mean: 99.7 ± 92.6 pg m^{-3}) exceeded those at most remote global sites. Consistently higher values were observed during the dry season compared to the wet season (Guo et al., 2022), with an estimated dry deposition flux of 15.7 μg m^{-2} yr^{-1}.

4.3 Hg from precipitation

Precipitation Hg measurements from multiple stations across the Third Pole reveal distinct spatial and temporal patterns (APCC dataset I-3). At Nam Co station, mean Hg_T concentrations measured 4.8 ng L^{-1} with a clear seasonal pattern showing two-fold higher levels during non-monsoon periods compared to monsoon seasons (Huang et al., 2012a). Despite lower concentrations, monsoon rainfall accounted for 83 ± 5% of annual wet deposition fluxes, demonstrating precipitation-driven scavenging efficiency. Speciation analysis showed Hg_P dominated precipitation Hg_T (71.2%), with MeHg constituting 1.82% of Hg_T.

The Lhasa station exhibited significantly higher Hg_T concentrations (24.8 ng L^{-1}) with different deposition dynamics (Huang et al., 2013). Here, Hg_T wet deposition flux was primarily concentration-driven rather than precipitation-dependent as observed at Nam Co. Seasonal variations showed higher Hg_T and Hg_P concentrations during non-monsoon periods, while reactive Hg (Hg_R) in precipitation peaked during monsoon seasons. Speciation indicated Hg_P accounted for 77% of Hg_T, with Hg_R representing only 5%.

In Southeast Tibet station, while mean Hg_T concentration (4.0 ng L^{-1}) was relatively low, MeHg levels (0.112 ng L^{-1}) and deposition flux (0.11 μg m^{-2} yr^{-1}) were among the highest reported globally (Huang et al., 2015). Hg_D emerged as the dominant species, suggesting significant contributions from gaseous oxidized Hg scavenging.

Expanded monitoring across 9 stations in both monsoon and westerlies domains across the Third Pole revealed contrasting regional patterns (Huang et al., 2022). The westerlies domain showed higher Hg_T concentrations and Hg_P percentages (Fig. 3a), while the monsoon domain exhibited greater deposition fluxes and MeHg levels (Fig. 3b). Extreme values were recorded at Motuo station in the Yarlung Tsangpo Grand Canyon (56.3 ng L^{-1} Hg_T concentration, 84.7 μg m^{-2} yr^{-1} flux) (Huang et al., 2024).

Nepal Himalayan measurements demonstrated strong spatial gradients, with Kathmandu showing urban-level Hg concentrations (34.91 μg m^{-2} yr^{-1} flux) compared to background sites like Dhunche

https://doi.org/10.5194/essd-2025-551
Preprint. Discussion started: 13 March 2026

(15.89 μg m^{-2} yr^{-1}) (Tripathee et al., 2019). All sites exhibited pronounced seasonal variability, with higher concentrations during non-monsoon periods (Tripathee et al., 2019, 2020).

4.4 Hg from glacier

Systematic snowpit surveys conducted at 9 glaciers (Fig. 1 and Table 2) between 2005-2010 revealed total Hg concentrations ranging from below detection limit (<1 ng L^{-1}) to 43.6 ng L^{-1} across all sampling sites (APCC I-4; Zhang et al., 2012). The seasonal amplitude of Hg concentrations showed winter maxima averaging 28.3 ± 8.7 ng L^{-1} compared to summer minima of 5.2 ± 3.1 ng L^{-1} (n = 14 snowpits). Spatial distribution patterns indicated 35-42% higher concentrations in northern glaciers (Xiao Dongkemadi, Laohugou No.12) relative to southern sites (East Rongbuk, Zhadang) (Figs. 1 and 4). Corresponding annual deposition fluxes varied from 0.74 ± 0.21 to 7.89 ± 2.34 μg m^{-2} yr^{-1} across different glaciers (Zhang et al., 2012).

Detailed analysis of July 2013 samples from Laohugou Glacier No. 12 (northeastern Tibetan Plateau) demonstrated Hg_P accounted for 82 ± 11% of total Hg in snow/ice matrices (APCC I-4; Huang et al., 2014b). Vertical snowpit profiles (n = 5) exhibited consistent Hg enrichment patterns, with concentration increasing from 3.2 ± 1.1 ng L^{-1} in surface layers to 18.6 ± 5.3 ng L^{-1} at 1.8 m depth (Huang et al., 2014b).

Surface snow sampling campaigns during 2008-2010 covered 4 high-altitude glaciers (East Rongbuk: 6,350 m; Zhadang: 5,800 m; Ganglongjiama: 5,600 m; Muztagata: 4,900 m), with mean elevation of 5,200 ± 620 m (APCC I-4; Huang et al., 2012b). Measured Hg concentrations showed site-specific variations: Mt. Muztagata (range: 2.1-15.0 ng L^{-1}; mean: 8.56 ± 3.72 ng L^{-1}) consistently displayed higher values than Mt. Nyainqêntanglha (0.9-3.2 ng L^{-1}; mean: 1.8 ± 0.7 ng L^{-1}). Mass balance calculations indicated 31 ± 9% of initially deposited Hg was lost during snow metamorphosis processes (Huang et al., 2012b).

Cryoconite samples collected from 7 glaciers (n = 112) revealed distinct spatial patterns in Hg accumulation (APCC I-4; Huang et al., 2019). Southern glaciers influenced by monsoon circulation (East Rongbuk, Ganglongjiama) showed higher mean Hg concentrations (66.0 ± 29.3 ng g^{-1}; range: 22-143 ng g^{-1}) compared to westerlies-dominated northern glaciers (Laohugou No.12, Muztagata: 42.5 ± 20.7 ng g^{-1}; range: 15-89 ng g^{-1}). MeHg was detected in all cryoconite samples (n = 112), with concentrations ranging from 0.3 to 2.1 ng g^{-1} (overall mean: 1.0 ± 0.4 ng g^{-1}) (Huang et al., 2019). Elevation-dependent trends exhibited contrasting correlations between northern and southern glacier sites, with northern regions showing a decreasing trend and southern regions displaying an increasing trend with elevation.

4.5 Hg from soil

Comprehensive soil sampling (n = 336) was conducted across 28 locations representing meadow (n = 84), grassland (n = 112), desert (n = 92), and forest (n = 48) ecosystems, covering an elevation range of 2,917-4,762 m across the Tibetan Plateau (Fig. 5). Hg concentrations showed considerable variability, ranging from 2.1 to 200.3 ng g^{-1} with an overall arithmetic mean of 31.8 ng g^{-1} (geometric mean: 22.4 ng g^{-1}) (APCC dataset I-5; Yin et al., 2024). Among ecosystem types, forest soils

https://doi.org/10.5194/essd-2025-551
Preprint. Discussion started: 13 March 2026

consistently exhibited the highest concentrations (range: 18.6-200.3 ng g^{-1}; mean: 74.4 ng g^{-1}), followed by meadow (mean: 29.2 ng g^{-1}), grassland (mean: 25.7 ng g^{-1}), and desert ecosystems (mean: 12.8 ng g^{-1}). Spatial interpolation analysis revealed a clear southeast-to-northwest decreasing gradient, with maximum values clustered in southeastern forested regions (Fig. 5; Yin et al., 2024).

Along a 1,200 km southwest-northeast transect across the Himalaya-Tibet region, soil Hg analysis of 31 samples showed distinct spatial variation (Huang et al., 2020b). Southern slope soils (n = 21 sampling sites) displayed higher and more variable concentrations (range: 15-189 ng g^{-1}; mean ± SD: 72 ± 54 ng g^{-1}) compared to northern slopes (n = 10 sites; range: 12-89 ng g^{-1}; mean ± SD: 43 ± 26 ng g^{-1}) (Huang et al., 2020b). In the central Himalayas (Langtang region), soil Hg measurements (n = 45) averaged 35.75 ± 24.41 ng g^{-1} (range: 8.2-112.3 ng g^{-1}), with a consistent negative correlation between concentration and elevation ($r = -0.63$, $p<0.01$) across the 3,800-5,200 m altitude range (Tripathee et al., 2018).

The Central Asia topsoil survey (0-10 cm depth) encompassed 182 sampling sites across three countries (Tajikistan: n = 67; Uzbekistan: n = 72; Kyrgyzstan: n = 43), representing five land use types (Fig. 6a). Hg concentrations showed extreme variability (1.6-908 ng g^{-1}), with urban areas exhibiting both the highest maximum values and greatest variability (range: 8.6-908 ng g^{-1}; mean ± SD: 79.8 ± 112.3 ng g^{-1}). Other land types showed progressively lower mean concentrations: woodland (n = 38; 27.3 ± 18.4 ng g^{-1}), grassland (n = 52; 20.6 ± 12.7 ng g^{-1}), farmland (n = 29; 18.3 ± 9.8 ng g^{-1}), and desert (n = 23; 12.3 ± 6.5 ng g^{-1}) (APCC dataset I-5; Yang et al., 2023). The spatial distribution showed clear hotspots in capital city regions, with 12 urban samples exceeding 200 ng g^{-1} (Fig. 6b).

4.6 Hg from surface water

Available surface water Hg measurements from various aquatic systems across the Third Pole, including lakes, rivers, and glacial meltwater, are summarized in Fig. 7. In the Yarlung Zangbo River basin, surface water samples collected from 17 sites along the upper/middle reaches and tributaries (Lhasa and Niyang rivers) showed Hg_T concentrations ranging from 1.46 to 4.99 ng L^{-1} (Zheng et al., 2010). Seasonal sampling in the Koshi River basin, significantly influenced by the South Asian monsoon, revealed Hg_T concentrations varying between 0.64 and 32.96 ng L^{-1} (mean: 5.83 ± 6.19 ng L^{-1}), with the highest values consistently observed during post-monsoon periods (Sun et al., 2020c). Hg_P accounted for more than 50% of Hg_T, particularly during and after monsoon seasons, indicating its dominant role in seasonal and spatial Hg variations.

Surface water samples from 42 Tibetan Plateau lakes exhibited Hg_T concentrations ranging from <1 to 40.3 ng L^{-1} (APCC dataset I-6; Li et al., 2015; Paudyal et al., 2019; Sun et al., 2023). The spatial distribution revealed a distinct northwest-southeast gradient, with higher concentrations generally observed in northwestern regions (Li et al., 2015). This comprehensive dataset provides valuable baseline information on Hg distribution patterns across different aquatic ecosystems in the Third Pole, documenting both spatial gradients and seasonal variations while maintaining focus on observational evidence.

Glacial meltwater measurements from 7 glacier runoffs (Laohugou No.12, Zhadang, Xiao Dongkemadi, Kuqionggangri, Qiangyong, Hailuogou, East Rongbu) during ablation periods showed

https://doi.org/10.5194/essd-2025-551
Preprint. Discussion started: 13 March 2026

Open Access Earth System Science Data Discussions

Hg_T concentrations generally below background levels, with peaks occurring during maximum melt periods (APCC dataset I-6). Some sites, such as Laohugou No.12, occasionally exceeded 100 ng L^{-1} (Wang et al., 2024). Downstream sampling at Zhadang glacier demonstrated increasing Hg transport with meltwater flow (Sun et al., 2017, 2018), while monthly observations at Rongbuk, Laohugou No.12, and Mingyong glaciers revealed temporal variations correlated with ablation intensity (Sun et al., 2022; Wang et al., 2022; Pu et al., 2024). The Qiangyong glacier basin showed a 20% decrease in Hg_T concentrations between proglacial lake inflow and outflow (APCC dataset I-6; Sun et al., 2016), suggesting lake systems may act as effective sinks for Hg transported by glacial meltwater.

4.7 Hg from glacier ice core and lake sediment cores

The Ganglongjiama (Guoqu) glacier ice core from Mt. Geladaindong provides a 500-year record of atmospheric Hg deposition, with concentrations ranging from <0.1 to 9.8 ng L^{-1} (mean: 0.84 ng L^{-1}) (APCC dataset I-7; Kang et al., 2016). Calculated deposition fluxes reveal distinct temporal patterns, with an overall mean of 0.36 μg m^{-2} yr^{-1}, increasing from 0.28 μg m^{-2} yr^{-1} in the pre-industrial period to 0.91 μg m^{-2} yr^{-1} in the post-WWII era (Fig. 8). These values are consistent with measurements from other Tibetan Plateau glaciers (Loewen et al., 2007; Zhang et al., 2012).

Lake sediment records demonstrate significant spatial variability across the Himalayas. Northern slope lakes (Qiangyong Co, Nam Co, Bangong Co, Lingge Co, Tanglha Lake) exhibit mean Hg concentrations of 36 ng g^{-1} (range: 7.6-119.8 ng g^{-1}), while southern slope lakes (Phewa, Gokyo, Gosainkunda) show higher values (mean: 103 ng g^{-1}; range: 6-647.7 ng g^{-1}) (Table 3). Post-WWII accumulation rates follow a similar pattern, with northern lakes averaging 14.6 μg m^{-2} yr^{-1} compared to 112.1 μg m^{-2} yr^{-1} in southern lakes (APCC dataset I-7; Kang et al., 2016).

The combined records document three temporal phases: (1) stable background levels (1500s-early 1800s), (2) initial increases (late 1800s), and (3) accelerated accumulation post-WWII (Figs. 8-9). Southern slope sediments consistently show 4-fold higher Hg concentrations and 8-fold greater deposition fluxes than northern counterparts (APCC dataset I-7; Kang et al., 2016). These patterns are preserved across different environmental archives, providing robust evidence of spatial and temporal variations in Hg deposition across the Himalayan region.

4.8 Hg stable isotopes from aerosol, soil and lake sediment

Hg isotope measurements (δ^{202}Hg, Δ^{199}Hg, Δ^{200}Hg) from various environmental media in the Third Pole provide insights into Hg sources and transport processes (Blum et al., 2014). Atmospheric aerosols in the Kathmandu Valley show δ^{202}Hg values ranging from -1.42‰ to 0.28‰ (mean: -0.82‰) and Δ^{199}Hg from -0.30‰ to -0.12‰ (mean: -0.16‰) (APCC dataset I-8; Guo et al., 2021). Seasonal variations were observed at LMB, with distinct isotopic signatures between pre-monsoon and monsoon periods (Guo et al., 2022).

Soil samples reveal a marked north-south contrast, with southern Himalayan slopes exhibiting lower mean δ^{202}Hg values (-0.53‰) compared to northern slopes (-0.12‰) (APCC dataset I-8; Huang et al., 2020b). Lake sediment cores from 4 lakes along a southwest-northeast transect show positive Δ^{199}Hg (0.07‰-0.44‰) and Δ^{200}Hg (0.03‰-0.08‰) values (APCC dataset I-8; Huang et al., 2023). The

https://doi.org/10.5194/essd-2025-551
Preprint. Discussion started: 13 March 2026

Δ^{199}Hg values peak at Tanglha Lake (0.44‰) before decreasing further northeast, suggesting a southwest-northeast gradient in isotopic composition. Lake sediment core records demonstrate a consistent increase in both δ^{202}Hg and Δ^{199}Hg values since the Industrial Revolution (Huang et al., 2020c), providing evidence for rising anthropogenic Hg emissions originating from South Asia. These isotopic measurements capture spatial patterns and variability in Hg signatures across diverse environmental compartments of the Third Pole. The dataset offers empirical constraints on Hg distribution, with an emphasis on observational evidence rather than source attribution.

5. Dataset limitations and applications

Research on Hg in the Third Pole faces major limitations that constrain the robustness and interpretability of available data. A primary challenge is the short-term, sporadic, and temporally inconsistent nature of existing measurements across different sites and seasons, resulting from extreme harsh environments, insufficient power supply stability, and severe logistical constraints-all of which preclude long-term or synchronous multi-site monitoring and impede the detection of coherent temporal trends and regional gradients. The sparse and geographically uneven distribution of monitoring stations, despite being strategically situated to represent specific local conditions, greatly reduces the capacity to evaluate the spatial representativeness of observed Hg dynamics across the topographically and ecologically heterogeneous Third Pole. Additional constraints include a general lack of standardized protocols for Hg sampling and analysis under cryospheric conditions, insufficiently resolved ancillary data (e.g., meteorology, aerosol chemistry), and limited integration with hydrological and ecological observations, which collectively hinder process-based understanding and model representation of Hg cycling in this sensitive and rapidly changing region.

This dataset enables high-time-resolution analysis of key biogeochemical processes-such as diurnal variations, deposition pulses, and post-depositional re-emission-across diverse cryospheric surfaces of the Third Pole, including glaciers, snow cover, and permafrost-affected areas. It supports improved understanding of Hg dynamics driven primarily by intense solar radiation, rapid freeze-thaw cycles, and temperature-sensitive redox changes, thereby offering significant potential for advancing Hg research in this critical environment. Despite the complex topography and sparse observatory coverage across the Third Pole, our spatially distributed observations enable comparative analysis of Hg transport and transformation processes across diverse cryospheric regimes. These data provide critical constraints for elucidating multifaceted Hg interactions (e.g., gas-aerosol, snow-air exchange) and significantly enhance the accuracy and mechanistic representation of atmospheric Hg models (e.g., GEOS-Chem, CMAQ-Hg) over high-altitude and heterogeneous terrains. Furthermore, the integration of atmospheric and cryospheric data supports investigation of deposition legacy, seasonal emission events, and Hg fate in meltwater and downstream ecosystems, making the dataset particularly relevant for assessing climate-cryosphere-Hg feedbacks under current and future warming scenarios.

6. Data availability

All the Hg dataset presented in this study can be downloaded from the Cold and Arid Regions Science Data Center at Lanzhou (https://www.doi.org/10.12072/ncdc.qzkk.db6654.2024, *Kang et al., 2024*).

A specific directory was designated with data classified into different categories:

https://doi.org/10.5194/essd-2025-551
Preprint. Discussion started: 13 March 2026

a) Real-time atmospheric Hg observation data (APCC dataset I-1),
b) Aerosol Hg data (APCC dataset I-2),
c) Precipitation Hg data (APCC dataset I-3),
d) Glacier (snowpit, surface snow, cryoconite) Hg data (APCC dataset I-4),
e) Soil Hg data (APCC dataset I-5),
f) River and lake water Hg data (APCC dataset I-6),
g) Ice and lake sediment cores Hg data (APCC dataset I-7),
h) Hg isotope data from aerosols, soils and lake sediments (APCC dataset I-8).

6. Conclusions

Based on the APCC program, a comprehensive Hg dataset has been assembled across the Third Pole. This study compiles measurements from diverse environmental matrices-including air, aerosols, precipitation, glaciers, soils, surface water, ice and lake sediment cores-encompassing Hg speciation, concentrations, fluxes, and isotopic compositions. The dataset represents a coordinated effort to address key scientific objectives, which include: (1) characterizing spatial, seasonal, and long-term variations of Hg across different environmental compartments in the Third Pole; (2) elucidating the processes and mechanisms governing transboundary transport and long-range deposition of atmospheric Hg into the region; (3) apportioning sources of atmospheric Hg using chemical tracers and modeling approaches, and identifying the fate of Hg within environmental media; and (4) improving predictions of Hg cycling in cryospheric environments and evaluating its impacts under rapid climate warming and cryospheric retreat. This information is essential for risk assessment and mitigation of Hg pollution at both global and regional scales, and provides scientific support for policy formulation.

Author contributions

SK, JH, QZ, JG, XY, SS, XS, LT, AS, WT, YZ, XM, LL and LC led the writing of the manuscript and endorsed the responsibility of experimental sites and instruments. SK and JH originally drafted the manuscript, and all of the authors contributed to the paper writing and data preparation. SK and JH led the consolidation of the dataset and prepared the data in the standardized format described in this paper together with all co-authors.

Competing interests

The authors declare that they have no conflict of interests.

Acknowledgements

Hg research team members in our research group (led by prof. Shichang Kang) are greatly appreciated for their efforts in participating field observations, maintaining the instruments, and analysing the samples in the laboratory.

Financial support

This work was supported bythe National Natural Science Foundation of China (42277397; 42571171), the Gansu Provincial Science and Technology Program (23ZDFA017; 24ZD13FA003), the

https://doi.org/10.5194/essd-2025-551
Preprint. Discussion started: 13 March 2026

606 Key Science and Technology Plan Project of Lhasa (Grant No. LSKJ202410), and the Key Research
607 and Development Program of Tibet Autonomous Region (Grant Nos. XZ202401ZY0068;
608 XZ202501ZY0078).
609

610 **Figures and tables:**

611 **Table 1** Detailed geographic characteristics of observation stations from the Atmospheric Pollution and Cryospheric
612 Change (APCC) program in this paper

Regions	Abbreviations	Site	Latitude (°N)	Longitude (°E)	Elevation (m a.s.l.)	Observations, Sample types
Tibetan Plateau	MZ	Muztagh Ata Station for Westerly Environment Observation and Research, Western Tibetan Plateau	38.291	75.055	5725	Muztagh Ata glacier, precipitation, snowpit, surface snow
	NA	Ngari Station for Desert Environment Observation and Research, Western Tibetan Plateau	33.392	79.701	4270	precipitation
	LHG	Qilian Observation and research Station of Cryosphere and Ecologic Environment, Northern Tibetan Plateau	39.429	96.556	4230	Laohugou glacier No.12/Shiyi glacier, precipitation, snowpit, surface snow, cryoconite, glacial meltwater
	TGL	Tanggula Cryosphere and Environment Observation Station, Central Tibetan Plateau	33.083	92.067	5000	Xiao Dongkemadi /Ganglongjiama (Guoqu) glaciers, air, snowpit, cryoconite
	NMC	Nam Co Station for Multisphere Observation and Research, Southern Tibetan Plateau	30.779	90.991	4730	Zhadang glacier, air, precipitation, snowpit, surface snow, cryoconite, glacial meltwater
	EV	Qomolangma Atmospheric and Environmental Observation and Research Station (Everest), Southern Tibetan Plateau	28.35	86.933	4276	East Rongbuk glacier, precipitation, snowpit, surface snow, glacial meltwater
	SET	South-East Tibetan plateau Station for integrated observation and research of alpine environment (Lulang), Southeast Tibetan Plateau	29.767	94.733	3326	Demula glaciers/Parlong glacier No. 4, precipitation, snowpit, cryoconite
	YL	Yulong Snow Mountain Glacial and Environmental Observation and Research Station, Southeastern Tibetan Plateau	27.167	100.167	2650	Baishui glacier No.1/ Mingyong/Hailuogou glaciers, precipitation, snowpit, cryoconite, glacial meltwater
	MT	The Motuo Observation and Research Center for Earth Landscape and Earth System of the Chinese Academy of Sciences, Southeast Tibetan Plateau	29.325	95.293	820	precipitation
	LS	Lhasa city, Tibet Autonomous Region	29.633	91.3	3642	Qiangyong/Kuoqionggangri glaciers, aerosol, precipitation, glacial meltwater

https://doi.org/10.5194/essd-2025-551
Preprint. Discussion started: 13 March 2026

Xinjiang	JMN	Altai Observation and Research Station of Cryospheric Science and Sustainable Development (Jimunai, Northern Xinjiang)	47.100	87.966	997	Muz Taw glacier, snowpit
	AK	Field Scientific Experiment Base of Akdala Atmospheric Background, China Meteorological Administration (Northern Xinjiang)	46.843	88.133	563	precipitation
	TS	Tianshan Glaciological Station, Central Xinjiang	43.105	86.807	2100	Urumqi glacier No.1, precipitation, snowpit, cryoconite
	KS	Kashgar, Southern Xinjiang	75.45	39.29	1386	aerosol
	MF	Minfeng, Southern Xinjiang	82.72	37.04	1410	aerosol
	TZ	Tazhong, Southern Xinjiang	83.39	38.58	1099	aerosol
	RQ	Ruoqiang, Eastern Xinjiang	88.10	39.02	889	aerosol
	TX	Taxkorgan, Southern Xinjiang	75.14	37.47	3094	aerosol
Nepal	DC	Dhunche	28.117	85.3	2065	precipitation
	DM	Dimsa	28.183	83.983	3078	precipitation
	PKR	Gosainkunda	28.095	85.65	4417	precipitation
	JMS	Jomsom	28.87	83.73	2750	precipitation
	BD	Bode, Kathmandu	27.683	85.4	1314	aerosol, precipitation
	DHK	Dhulikhel, Kathmandu	27.619	85.538	1514	aerosol
	LMB	Lumbini	27.483	83.283	100	aerosol

https://doi.org/10.5194/essd-2025-551
Preprint. Discussion started: 13 March 2026

Table 2 Detailed information for the observed glaciers based on the APCC program in this paper

Regions	Mountains	Glacier name	Latitude	Longitude
Southeastern Tibetan Plateau	Hengduan Mts.	Baishui glacier No.1	27.17°N	100.15°E
Southeastern Tibetan Plateau	Hengduan Mts.	Mingyong glacier	28.468°N	98.799°E
Southeastern Tibetan Plateau	Hengduan Mts.	Hailuogou glacier	29.566°N	102.001°E
Southeastern Tibetan Plateau	Gangrigabu Mts.	Demula glacier	29.355°N	97.02°E
Southeastern Tibetan Plateau	Gangrigabu Mts.	Parlung glacier No.4	29.233°N	90.633°E
Southeastern Tibetan Plateau	Eastern Himalayas	Qiangyong glacier	28.883°N	90.217°E
Inland Tibetan Plateau	Nyainqengtanglha Mts.	Zhadang glacier glacier	30.467°N	90.633°E
Inland Tibetan Plateau	Nyainqengtanglha Mts.	Kuoqionggangri glacier	29.870°N	90.211°E
Inland Tibetan Plateau	Tanggulha Mts.	Xiao Dongkemadi glacier	33.066°N	92.066°E
Inland Tibetan Plateau	Tanggulha Mts.	Ganglongjiama glacier (Guoqu glacier)	33.833°N	91.683°E
Northern Tibetan Plateau	Qilian Mts.	Laohugou glacier No.12	39.44°N	96.542°E
Northern Tibetan Plateau	Qilian Mts.	Shiyi glacier	38.35°N	100.466°E
Himalayas	Mt. Everest	East Rongbuk glacier	28.031°N	86.961°E
Xinjiang	Eastern Tianshan	Urumqi glacier No.1	43.116°N	86.8°E
Xinjiang	Sawir Mts.	Muz Taw glacier	47.06°N	85.56°E
Xinjiang	Mt. Muztagh	Muztagh Ata glacier	38.283°N	75.067°E

Note: An ice core with depth of 147 m was collected in 2005 from the upper basin of the Ganglongjiama glacier (Guoqu glacier, 33.58°N, 91.18°E; 5750 m a.s.l.) on the northern slope of the Mt. Geladaindong. Mts.: Mountains

Table 3 Detailed information for the lake sediments cores in this paper

Regions	Lake name	Latitude (N)	Longitude (E)	Elevation (m a.s.l.)
Tibetan Plateau	Qiangyong Co	28°53.409'	90°13.558'	4866
	Nam Co	30°49.269'	90°48.788'	4710
	Tanggula	32°54.209'	91°57.162'	5152
	Lingg Co	33°49.85'	88°36.15'	5051
	Bangong Co	33°31.2'	79°49.1'	4240
Nepal	Gokyo	27°57.063'	86°41.414'	4750
	Phewa	28°12.72'	83°56.779'	793
	Gosainkunda	28°5.717'	85°39.017'	4390

https://doi.org/10.5194/essd-2025-551
Preprint. Discussion started: 13 March 2026

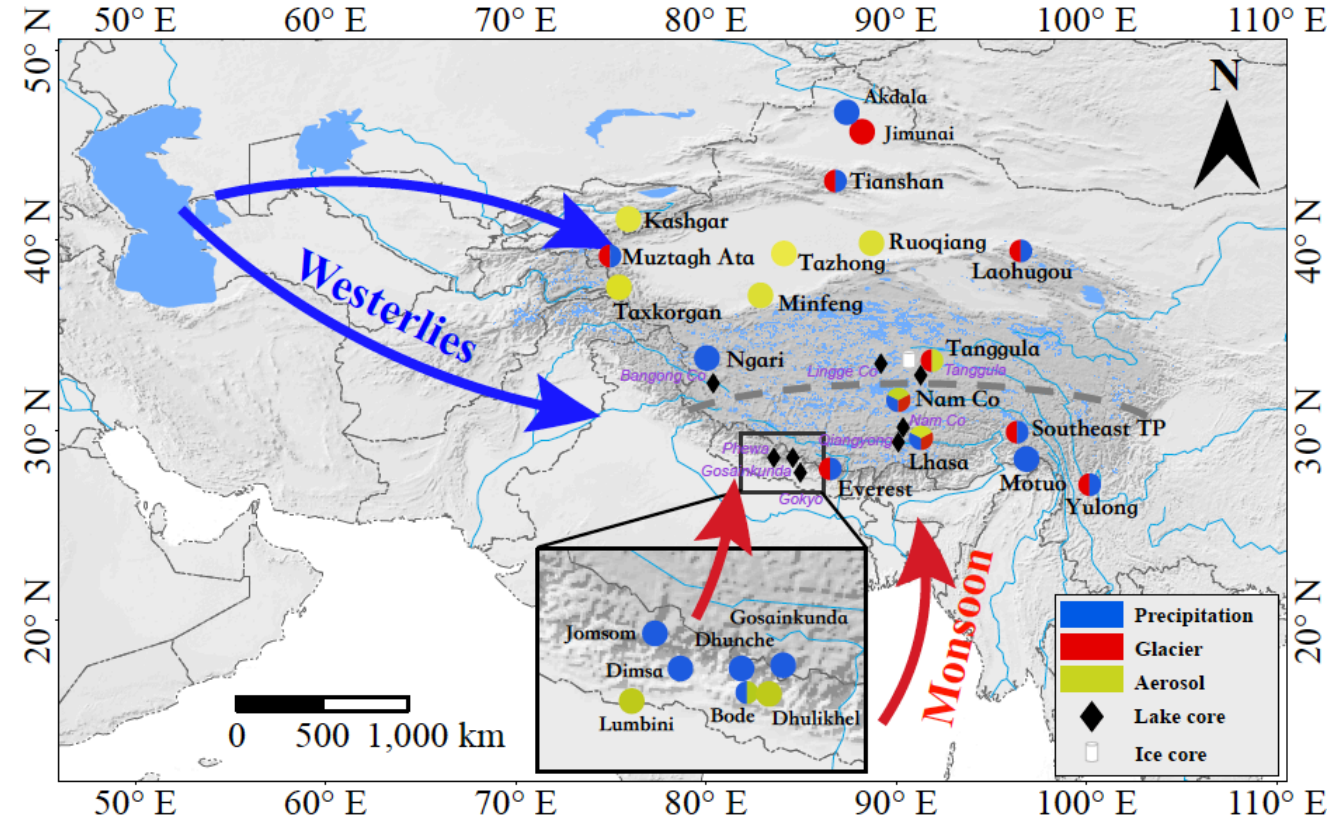

Figure 1. A map of the Third Pole, showing the geographical locations of the observation sites (see Table 1 for the detailed information of each station) from the Atmospheric Pollution and Cryospheric Change (APCC) program. Also shown are the general patterns of atmospheric circulation systems. The gray dashed line shows the northern boundary of the India monsoon based on seasonal $\delta^{18}O$ changes in precipitation (Tian et al., 2007), which divides the Tibetan Plateau into the monsoon domain in the south and the westerlies domain in the north.

https://doi.org/10.5194/essd-2025-551
Preprint. Discussion started: 13 March 2026

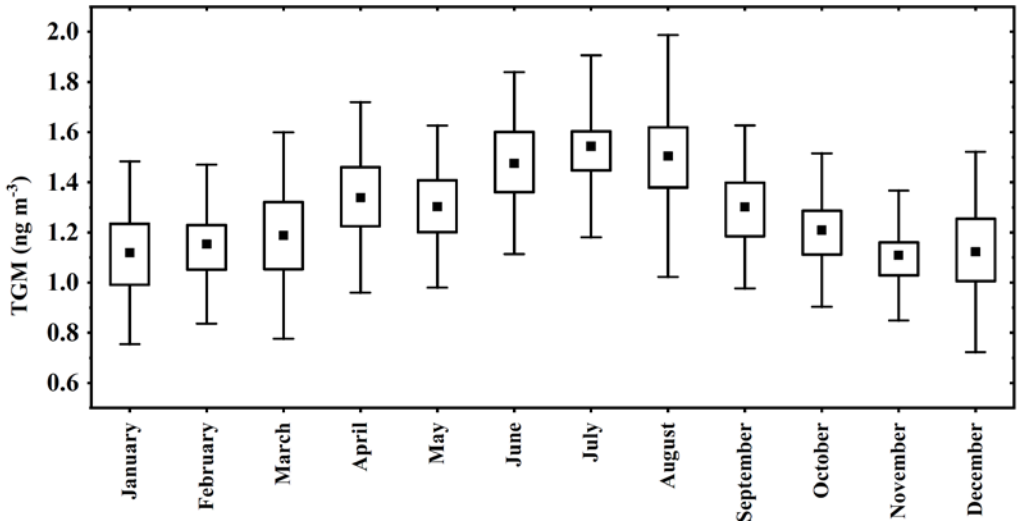

Figure 2. Monthly average of TGM at Nam Co Station during the whole measurement period. Source: X. Yin et al. (2018).

https://doi.org/10.5194/essd-2025-551
Preprint. Discussion started: 13 March 2026

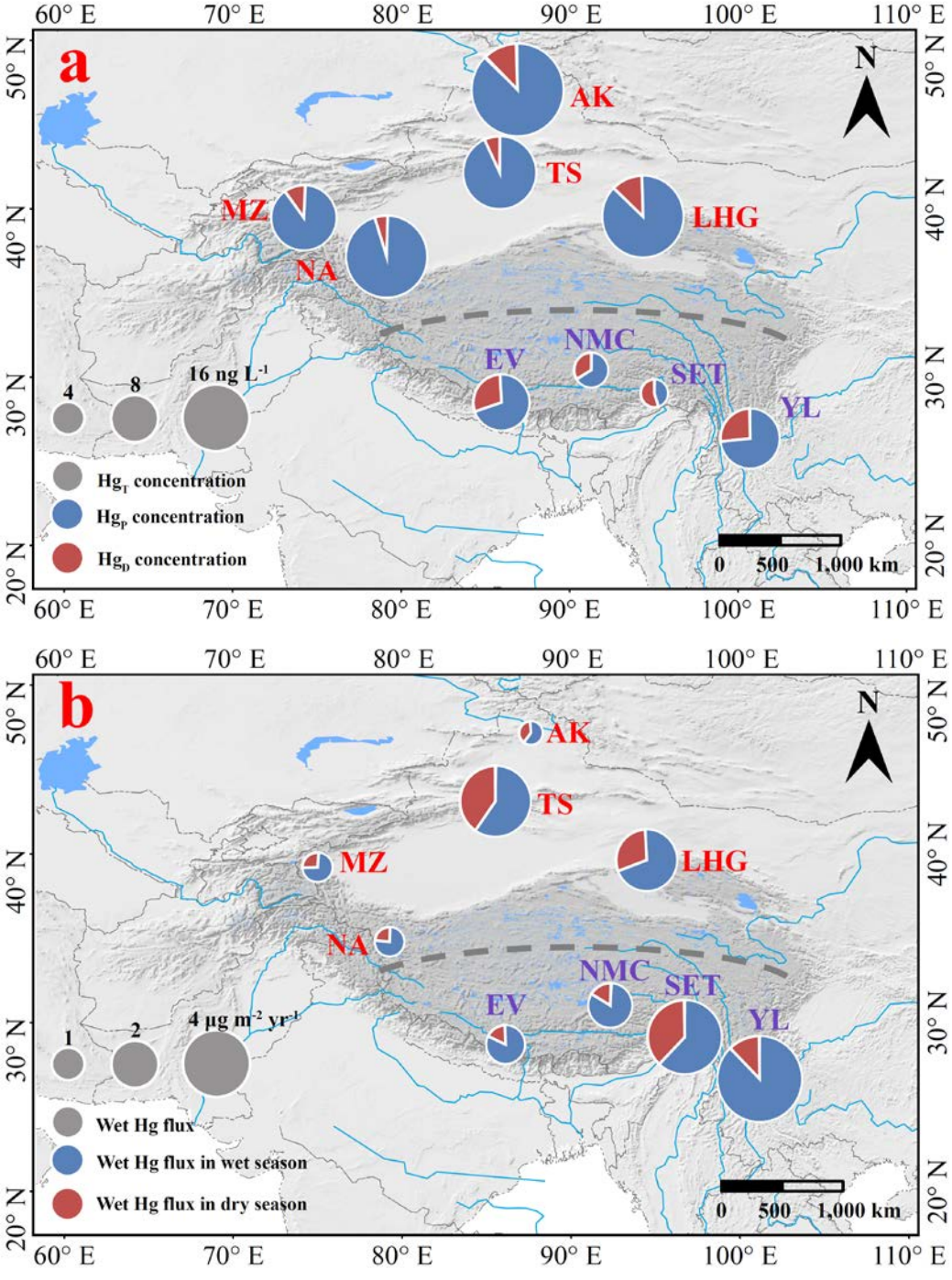

Figure 3. Spatial distribution of precipitation Hg concentration (a) and wet Hg deposition flux (b) between the monsoon and westerlies domains over the Third Pole (Acronyms are as same as Table 1). Source: J. Huang et al. (2022).

https://doi.org/10.5194/essd-2025-551
Preprint. Discussion started: 13 March 2026

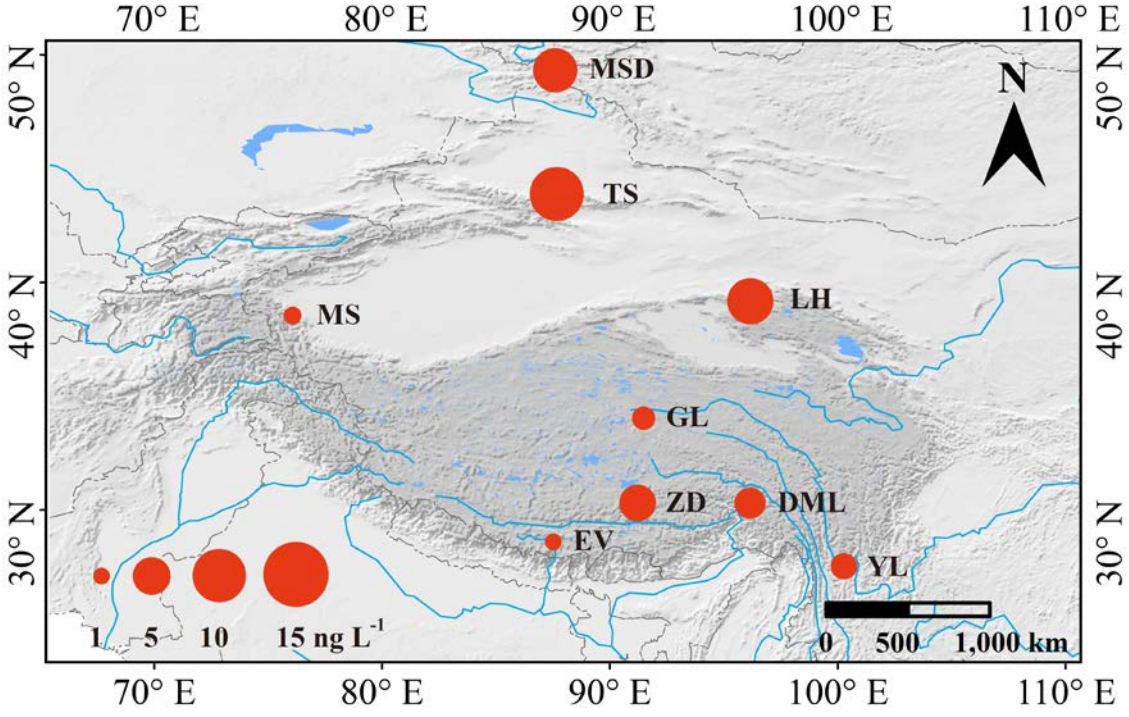

Figure 4. The red circle shows the location of the glacier sampling sites over the Third Pole, while its area represents the average Hg_T concentrations from the glacier snowpits (Acronyms are as same as Table 1). Source: Q. Zhang et al. (2012).

https://doi.org/10.5194/essd-2025-551
Preprint. Discussion started: 13 March 2026

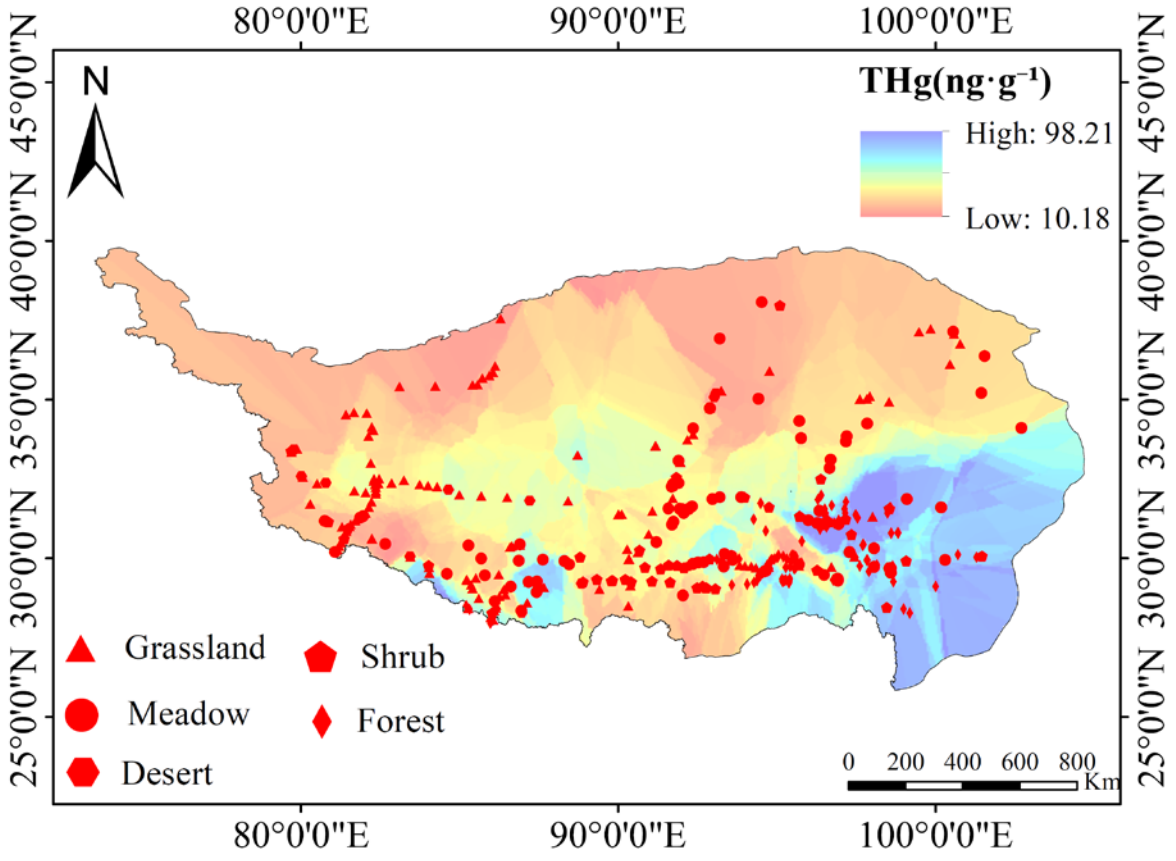

Figure 5. Spatial distribution of topsoil Hg_T concentrations across the Tibetan Plateau. The map, based on 336 topsoil samples from meadow, grassland, desert, and forest ecosystems, reveals a distinct southeast-to-northwest decreasing gradient, with the highest concentrations in the southeastern forested regions. Source: X. Yin et al. (2024).

https://doi.org/10.5194/essd-2025-551
Preprint. Discussion started: 13 March 2026

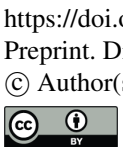

Open Access Earth System Science Data Discussions

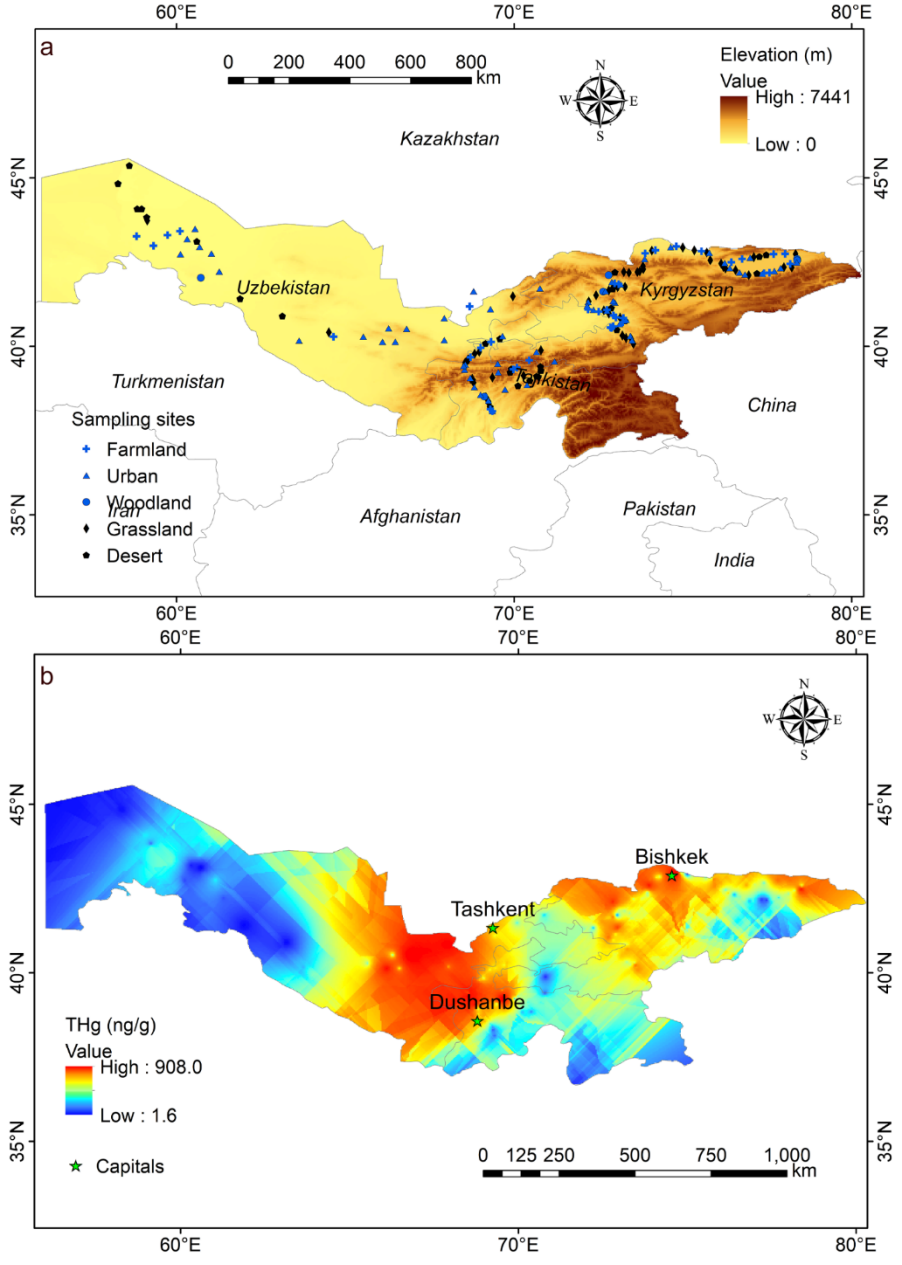

Figure 6. (a) Topsoil sampling sites and (b) spatial distribution of Hg_T concentrations in topsoils (0-10 cm) across Central Asia. Results from 182 sites show extreme variability (1.6-908 ng g^{-1}), with pronounced urban hotspots-particularly in capital cities-driving the spatial distribution pattern. Source: Z. Yang et al. (2023).

https://doi.org/10.5194/essd-2025-551
Preprint. Discussion started: 13 March 2026

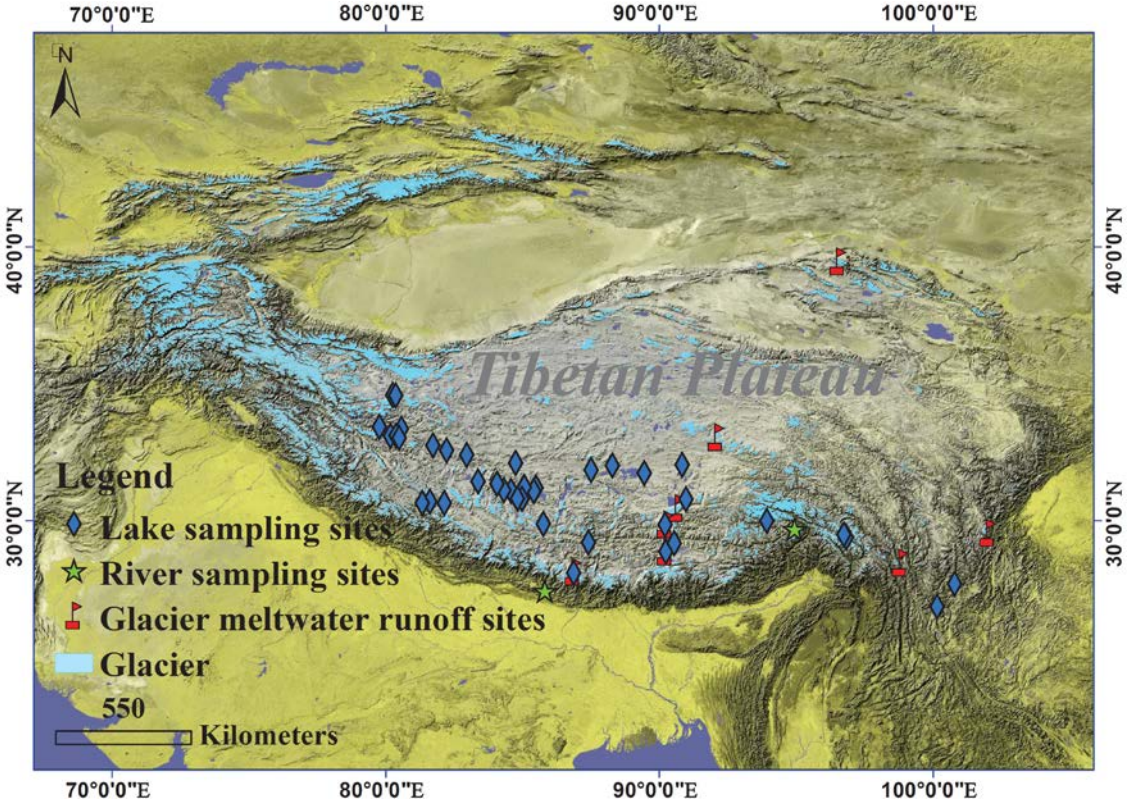

Figure 7. Sampling sites and compiled measurements of Hg_T in surface waters (rivers, lakes, glacier runoffs) across the Third Pole. Data in section 4.6 reveal a northwest-southeast increasing gradient in lakes, seasonal peaks in post-monsoon rivers with Hg_P as the dominant form, and generally low but temporally variable Hg_T in glacial meltwater, influenced by ablation intensity and downstream processes.

https://doi.org/10.5194/essd-2025-551
Preprint. Discussion started: 13 March 2026

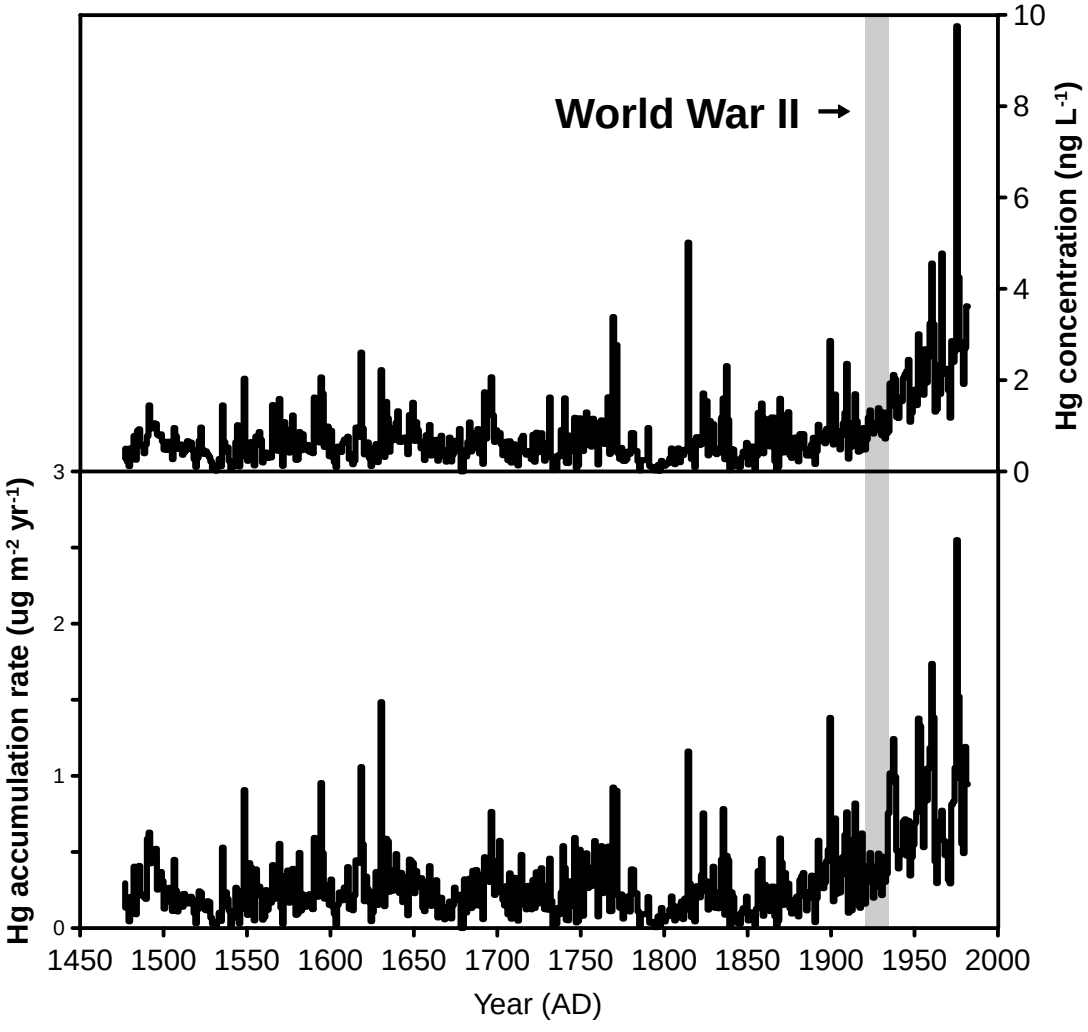

Figure 8. Historical trends of concentration and accumulation rate of Hg reconstructed from the Geladaindong ice core (contours indicate the year-by-year variability; gray bar represents the World War II period). Source: S. Kang et al. (2016).

https://doi.org/10.5194/essd-2025-551
Preprint. Discussion started: 13 March 2026

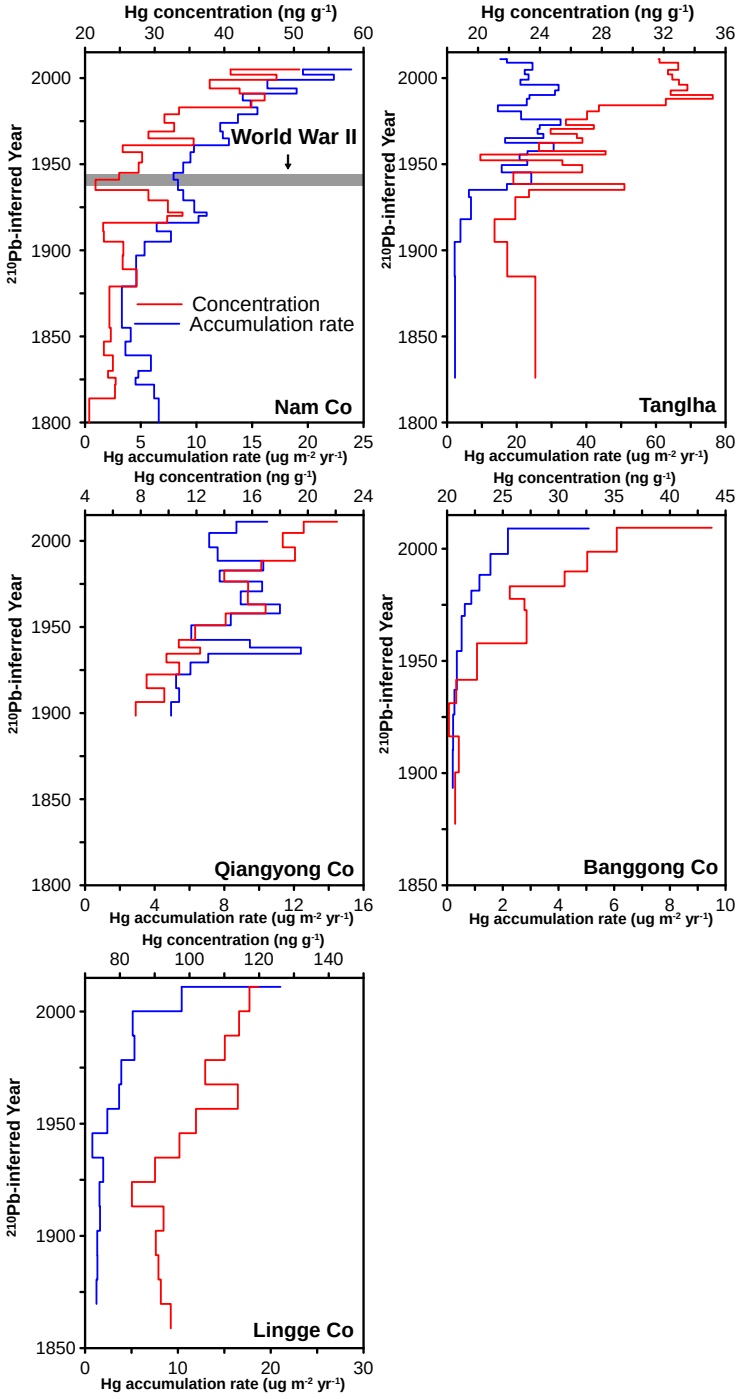

Figure 9. Hg concentration and accumulation rate profiles of the sediment cores taken from five lakes (Qiangyong Co, Nam Co, Bangong Co, Lingge Co, and Tanglha Lake) in the northern slopes of the Himalayas. Gray bar represents the World War II period. Source: S. Kang et al. (2016).

https://doi.org/10.5194/essd-2025-551
Preprint. Discussion started: 13 March 2026

References

Beckers, F., and Rinklebe, J.: Cycling of mercury in the environment: Sources, fate, and human health implications: A review. Crit.Rev. Env. Sci. Tec. 47, 693-794, https://doi.org/10.1080/10643389.2017.1326277, 2017.

Bergquist, B.A., and Blum, J.D.: Mass-dependent and-independent fractionation of Hg isotopes by photoreduction in aquatic systems. Science 318, 417-420, https://doi.org/10.1126/science.1148050, 2007.

Blum, J.D., Sherman, L.S., and Johnson, M.W.: Mercury isotopes in earth and environmental sciences. Annu. Rev. Earth Planet. Sci. 42, 249-269, https://doi.org/10.1146/annurev-earth-050212-124107, 2014.

Chen, D., Xu, B., Yao, T., Guo, Z., Cui, P., Chen, F., Zhang, R., Zhang, X., Zhang, Y., Fan, J., Hou, Z., and Zhang, T.: Assessment of past, present and future environmental changes on the Tibetan Plateau. Chin. Sci. Bull. 60(32), 3025-3035, https://doi.org/10.1360/N972014-01370, 2015.

de Foy, B., Tong, Y., Yin, X., Zhang, W., Kang, S., Zhang, Q., Zhang, G., Wang, X., and Schauer, J.J.: First field-based atmospheric observation of the reduction of reactive mercury driven by sunlight. Atmos. Environ. 134, 27-39, https://doi.org/10.1016/j.atmosenv.2016.03.028, 2016.

Driscoll, C.T., Mason, R.P., Chan, H.M., Jacob, D.J., and Pirrone, N.: Mercury as a global pollutant: sources, pathways, and effects. Environ. Sci. Technol. 47, 4967-4983, https://doi.org/10.1021/es305071v, 2013.

Grandjean, P., Satoh, H., Murata, K., and Eto, K.: Adverse effects of methylmercury: Environmental health research implications. Environ. Health Persp. 118, 1137-1145, https://doi.org/10.1289/ehp.0901757, 2010.

Guo, J., Kang, S., Huang, J., Zhang, Q., Rupakheti, M., Sun, S., Tripathee, L., Rupakheti, D., Panday, A.K., and Sillanpää, M.: Characterizations of atmospheric particulate-bound mercury in the Kathmandu Valley of Nepal, South Asia. Sci. Total Environ. 579, 1240-1248, https://doi.org/10.1016/j.scitotenv.2016.11.110, 2017.

Guo, J., Sharma, C.M., Tripathee, L., Kang, S., Fu, X., Huang, J., Shrestha, K.L., and Chen, P.: Source identification of atmospheric particle-bound mercury in the Himalayan foothills through non-isotopic and isotope analyses. Environ. Pollut. 286, 117317, https://doi.org/10.1016/j.envpol.2021.117317, 2021.

Guo, J., Tripathee, L., Kang, S., Zhang, Q., Huang, J., Mani Sharma, C., Chen, P., Paudyal, R., and Rupakheti, D.: Atmospheric particle-bound mercury in the northern Indo-Gangetic Plain region: Insights into sources from mercury isotope analysis and influencing factors. Geosci. Front. 13, 101274, https://dx.doi.org/10.1016/j.gsf.2021.101274, 2022.

Huang, J., Kang, S., Zhang, Q., Yan, H., Guo, J., Jenkins, M.G., Zhang, G., and Wang, K.: Wet deposition of mercury at a remote site in the Tibetan Plateau: Concentrations, speciation, and fluxes. Atmos. Environ. 62, 540-550, https://doi.org/10.1016/j.atmosenv.2012.09.003, 2012a.

Huang, J., Kang, S., Zhang, Q., Jenkins, M., Guo, J., Zhang, G., and Wang, K.: Spatial distribution and magnification processes of mercury in snow from high-elevation glaciers in the Tibetan Plateau. Atmos. Environ. 46, 140-146, https://doi.org/10.1016/j.atmosenv.2011.10.008, 2012b.

Huang, J., Kang, S., Wang, S., Wang, L., Zhang, Q., Guo, J., Wang, K., Zhang, G., and Tripathee, L.: Wet deposition of mercury at Lhasa, the capital city of Tibet. Sci. Total Environ. 447, 123-132, https://doi.org/10.1016/j.scitotenv.2013.01.003, 2013.

Huang, J., Kang, S., Guo, J., Sillanpää, M., Zhang, Q., Qin, X., Du, W., and Tripathee, L.: Mercury distribution and variation on a high-elevation mountain glacier on the northern boundary of the Tibetan Plateau. Atmos. Environ. 96, 27-36, https://doi.org/10.1016/j.atmosenv.2014.07.023, 2014b.

https://doi.org/10.5194/essd-2025-551
Preprint. Discussion started: 13 March 2026

Huang, J., Kang, S., Zhang, Q., Guo, J., Sillanpää, M., Wang, Y., Sun, S., Sun, X., and Tripathee, L.: Characterizations of wet mercury deposition on a remote high-elevation site in the southeastern Tibetan Plateau. Environ. Pollut. 206, 518-526, https://doi.org/10.1016/j.envpol.2015.07.024, 2015.

Huang, J., Kang, S., Guo, J., Zhang, Q., Cong, Z., Sillanpää, M., Zhang, G., Sun, S., and Tripathee, L.: Atmospheric particulate mercury in Lhasa city, Tibetan Plateau. Atmos. Environ. 142, 433-441, https://doi.org/10.1016/j.atmosenv.2016.08.021, 2016.

Huang, J., Kang, S., Ma, M., Guo, J., Cong, Z., Dong, Z., Yin, R., Xu, J., Tripathee, L., Ram, K., and Wang, F.: Accumulation of atmospheric mercury in glacier cryoconite over western China. Environ. Sci. Technol. 53, 6632-6639, https://pubs.acs.org/doi/abs/10.1021/acs.est.8b06575, 2019.

Huang, J., Kang, S., Yin, R., Ram, K., Liu, X., Lu, H., Guo, J., Chen, S., and Tripathee, L.: Desert dust as a significant carrier of atmospheric mercury. Environ. Pollut. 267, 115442, https://doi.org/10.1016/j.envpol.2020.115442, 2020a.

Huang, J., Kang, S., Yin, R., Guo, J., Lepak, R., Mika, S., Tripathee, L., and Sun, S.: Mercury isotopes in frozen soils reveal transboundary atmospheric mercury deposition over the Himalayas and Tibetan Plateau. Environ. Pollut. 256, 113432, https://doi.org/10.1016/j.envpol.2019.113432, 2020b.

Huang, J., Kang, S., Yin, R., Lin, M., Guo, J., Ram, K., Li, C., Sharma, C., Tripathee, L., Sun, S., and Wang, F.: Decoupling natural and anthropogenic mercury and lead transport from South Asia to the Himalayas. Environ. Sci. Technol. 54, 5429-5436, https://pubs.acs.org/doi/10.1021/acs.est.0c00429?goto=supporting-info, 2020c.

Huang, J., Kang, S., Wang, L., Liu, K., Ram, K., Sillanpää, M., Tang, W., Guo, J., Zhang, Q., Ma, M., Tripathee, L., and Wang, F.: Anthropogenic and natural drivers of seesaw-like spatial patterns in precipitation mercury over western China. Environ. Pollut. 307, 119525, https://doi.org/10.1016/j.envpol.2022.119525, 2022.

Huang, J., Kang, S., Feng, X., Tang, W., Ram, K., Guo, J., Zhang, Q., Sharma, C.M., Li, C., Tripathee, L., and Wang, F.: Northward extent of atmospheric mercury transboundary transport to the Himalayas and Tibetan Plateau Region. Geophys. Res. Lett. 50, e2022GL100948, https://doi.org/10.1029/2022GL100948, 2023.

Huang, J., Zhang, Y., Kang, S., Tang, W., Liu, J., Liu, K., Wang, L., Guo, J., Tripathee, L., and Zhao, W.: Unexpectedly high wet mercury deposition observed in the Yarlung Tsangpo Grand canyon. Appl. Geochem. 175, 106175, https://doi.org/10.1016/j.apgeochem.2024.106175, 2024.

Immerzeel, W.W., Van Beek, L.P., and Bierkens, M.F.: Climate change will affect the Asian water towers. Science 328, 1382-1385, https://doi.org/10.1126/science.1183188. 2010.

Kang, S., Xu, Y., You, Q., Flügel, W.A., Pepin, N., and Yao, T.: Review of climate and cryospheric change in the Tibetan Plateau. Environ. Res. Lett. 5, 015101, https://doi.org/10.1088/1748-9326/5/1/015101, 2010.

Kang, S., Huang, J., Wang, F., Zhang, Q., Zhang, Y., Li, C., Wang, L., Chen, P., Sharma, C.M., and Li, Q.: Atmospheric mercury depositional chronology reconstructed from lake sediments and ice core in the Himalayas and Tibetan Plateau. Environ. Sci. Technol. 50, 2859-2869, https://doi.org/10.1021/acs.est.5b04172, 2016.

Kang, S., Zhang, Q., Qian, Y., Ji, Z., Li, C., Cong, Z., Zhang, Y., Guo, J., Du, W., Huang, J., You, Q., Panday, A.K., Rupakheti, M., Chen, D., Gustafsson, Ö., Thiemens, M.H., and Qin, D.: Linking atmospheric pollution to cryospheric change in the Third Pole region: current progress and future prospects. Natl. Sci. Rev. 6, 796-809, https://doi.org/10.1093/nsr/nwz031, 2019.

Kang S., Huang J., Zhang Q., Guo J., Yin X., Sun S., and Sun X.: Mercury Dataset of the Third Pole (2010-2023). National Cryosphere Desert Data Center, https://www.doi.org/10.12072/ncdc.qzkk.db6654.2024, 2024.

https://doi.org/10.5194/essd-2025-551
Preprint. Discussion started: 13 March 2026

Kessler, R.: The Minamata Convention on Mercury: a first step toward protecting future generations. Environ. Health Persp. 121, A304-A309, https://doi.org/10.1289/ehp.121-A304, 2013.

Kim, K.H., Kabir, E., and Jahan, S.A.: A review on the distribution of Hg in the environment and its human health impacts. J. Hazard. Mater. 306, 376-385, https://doi.org/10.1016/j.jhazmat.2015.11.031, 2016.

Li, C., Zhang, Q., Kang, S., Liu, Y., Huang, J., Liu, X., Guo, J., Wang, K., and Cong, Z.: Distribution and enrichment of mercury in Tibetan lake waters and their relations with the natural environment. Environ. Sci. Pollut. Res. 22, 12490-12500, https://doi.org/10.1007/s11356-015-4498-3, 2015.

Lin, C.J., Pan, L., Streets, D.G., Shetty, S.K., Jang, C., Feng, X., Chu, H.W., and Ho, T.C.: Estimating mercury emission outflow from East Asia using CMAQ-Hg. Atmos. Chem. Phys. 10, 1853-1864, https://doi.org/10.5194/acp-10-1853-2010, 2010.

Loewen, M., Kang, S., Armstrong, D., Zhang, Q., Tomy, G., and Wang, F.: Atmospheric transport of mercury to the Tibetan Plateau. Environ. Sci. Technol. 41, 7632-7638, https://doi.org/10.1021/es0710398, 2007.

Mergler, D., Anderson, H.A., Chan, L.H.M., Mahaffey, K.R., Murray, M., Sakamoto, M., and Stern, A.H.: Methylmercury exposure and health effects in humans: a worldwide concern. Ambio 36, 3-11, https://doi.org/10.1579/0044-7447(2007)36[3:meahei]2.0.co;2, 2007.

Paudyal, R., Kang, S., Huang, J., Tripathee, L., Zhang, Q., Li, X., Guo, J., Sun, S., He, X., and Sillanpää, M.: Insights into mercury deposition and spatiotemporal variation in the glacier and melt water from the central Tibetan Plateau. Sci. Total Environ. 599-600, 2046-2053, https://doi.org/10.1016/j.scitotenv.2017.05.145, 2017.

Paudyal, R., Kang, S., Tripathee, L., Guo, J., Sharma, C.M., Huang, J., Niu, H., Sun, S., and Pu, T.: Concentration, spatiotemporal distribution, and sources of mercury in Mt. Yulong, a remote site in southeastern Tibetan Plateau. Environ. Sci. Pollut. Res. 26, 16457-16469, https://doi.org/10.1007/s11356-019-05005-4, 2019.

Pu, T., Kong, Y., Kang, S., Wang, S., Guo, J., Jia, J., Wu, K., Shi, X., Wang, K., Sun, S., and Li, W.: Mercury export from a glacier-fed river of Mt. Meili, southeastern Tibetan Plateau. J. Hazard. Mater. 477, 135306, https://doi.org/10.1016/j.jhazmat.2024.135306, 2024.

Selin, H., Keane, S.E., Wang, S., Selin, N.E., Davis, K., and Bally, D.: Linking science and policy to support the implementation of the Minamata Convention on Mercury. Ambio 47, 198-215, https://doi.org/10.1007/s13280-017-1003-x, 2018.

Sprovieri, F., Pirrone, N., Bencardino, M., D'Amore, F., Carbone, F., Cinnirella, S., Mannarino, V., Landis, M., Ebinghaus, R., Weigelt, A., Brunke, E.-G., Labuschagne, C., Martin, L., Munthe, J., Wängberg, I., Artaxo, P., Morais, F., Barbosa, H. D. M. J., Brito, J., Cairns, W., Barbante, C., Diéguez, M. D. C., Garcia, P. E., Dommergue, A., Angot, H., Magand, O., Skov, H., Horvat, M., Kotnik, J., Read, K. A., Neves, L. M., Gawlik, B. M., Sena, F., Mashyanov, N., Obolkin, V., Wip, D., Feng, X. B., Zhang, H., Fu, X., Ramachandran, R., Cossa, D., Knoery, J., Marusczak, N., Nerentorp, M., and Norstrom, C.: Atmospheric mercury concentrations observed at ground-based monitoring sites globally distributed in the framework of the GMOS network, Atmos. Chem. Phys., 16, 11915–11935, https://doi.org/10.5194/acp-16-11915-2016, 2016.

Sun, R., Sun, G., Kwon, S.Y., Feng, X., Kang, S., Zhang, Q., Huang, J., and Yin, R.: Mercury biogeochemistry over the Tibetan Plateau: An overview. Crit. Rev. Environ. Sci. Technol. 1-26, https://doi.org/10.1080/10643389.2020.1733894, 2020a.

Sun, S., Kang, S., Huang, J., Li, C., Guo, J., Zhang, Q., Sun, X., and Tripathee, L.: Distribution and transportation of mercury from glacier to lake in the Qiangyong Glacier Basin, southern Tibetan Plateau, China. J. Environ. Sci. 44, 213-223, https://doi.org/10.1016/j.jes.2015.09.017, 2016.

https://doi.org/10.5194/essd-2025-551
Preprint. Discussion started: 13 March 2026

Sun, S., Ma, M., He, X., Obrist, D., Zhang, Q., Yin, X., Sun, T., Huang, J., Guo, J., Kang, S., and Qin, D.: Vegetation mediated mercury flux and atmospheric mercury in the alpine permafrost region of the central Tibetan Plateau. Environ. Sci. Technol. 54, 6043-6052, https://doi.org/10.1021/acs.est.9b06636, 2020b.

Sun, X., Wang, K., Kang, S., Guo, J., Zhang, G., Huang, J., Cong, Z., Sun, S., and Zhang, Q.: The role of melting alpine glaciers in mercury export and transport: An intensive sampling campaign in the Qugaqie Basin, inland Tibetan Plateau. Environ. Pollut. 220, 936-945, https://doi.org/10.1016/j.envpol.2016.10.079, 2017.

Sun, X., Zhang, Q., Kang, S., Guo, J., Li, X., Yu, Z., Zhang, G., Qu, D., Huang, J., Cong, Z., and Wu, G.: Mercury speciation and distribution in a glacierized mountain environment and their relevance to environmental risks in the inland Tibetan Plateau. Sci. Total Environ. 631-632, 270-278, https://doi.org/10.1016/j.scitotenv.2018.03.012, 2018.

Sun, X., Zhang, Q., Li, M., Kandel, K., Rawat, B., Pandey, A., Guo, J., Kang, S., Pant, R.R., Cong, Z., and Zhang, F.: Mercury variation and export in trans-Himalayan rivers: Insights from field observations in the Koshi River. Sci. Total Environ. 738, 139836, https://doi.org/10.1016/j.scitotenv.2020.139836, 2020c.

Sun, X., Zhang, Q., Zhang, G., Li, M., Li, S., Guo, J., Dong, H., Zhou, Y., Kang, S., Wang, X., and Shi, J.: Melting Himalayas and mercury export: Results of continuous observations from the Rongbuk Glacier on Mt. Everest and future insights. Water Res. 218, 118474, https://doi.org/10.1016/j.watres.2022.118474, 2022.

Sun, X., Zhang, Q., Li, M., Wang, J., Lu, Z., Guo, J., Kang, S., and Shi, J.: Insight into the relationships between total suspended particles and mercury in meltwater in a typical glacierized basin in the inland Tibetan Plateau. J. Hazard. Mater. 452, 131250, https://doi.org/10.1016/j.jhazmat.2023.131250, 2023.

Tian, L., Yao, T., MacClune, K., White, J.W.C., Schilla, A., Vaughn, B., Vachon, R., and Ichiyanagi, K.: Stable isotopic variations in west China: A consideration of moisture sources. J. Geophys. Res. 112, D10112, https://doi.org/10.1029/2006JD007718, 2007.

Tong, Y., Yin, X., Lin, H., Buduo, Danzeng, Wang, H., Deng, C., Chen, L., Li, J., Zhang, W., Schauer, J.J., Kang, S., Zhang, G., Bu, X., Wang, X., and Zhang, Q.: Recent decline of atmospheric mercury recorded by androsace tapete on the Tibetan Plateau. Environ. Sci. Technol. 50, 13224-13231, https://doi.org/10.1021/acs.est.6b04632, 2016.

Tripathee, L., Guo, J., Kang, S., Paudyal, R., Huang, J., Sharma, C.M., Zhang, Q., Rupakheti, D., Chen, P., Sharma Ghimire, P., and Gyawali, A.: Concentration and risk assessments of mercury along the elevation gradient in soils of Langtang Himalayas, Nepal. Hum. Ecol. Risk Assess. 1-12, https://doi.org/10.1080/10807039.2018.1459180, 2018.

Tripathee, L., Guo, J., Kang, S., Paudyal, R., Huang, J., Sharma, C.M., Zhang, Q., Chen, P., Ghimire, P.S., and Sigdel, M.: Spatial and temporal distribution of total mercury in atmospheric wet precipitation at four sites from the Nepal-Himalayas. Sci. Total Environ. 655, 1207-1217., https://doi.org/10.1016/j.scitotenv.2018.11.338, 2019.

Tripathee, L., Guo, J., Kang, S., Paudyal, R., Sharma, C.M., Huang, J., Chen, P., Sharma Ghimire, P., Sigdel, M., and Sillanpää, M.: Measurement of mercury, other trace elements and major ions in wet deposition at Jomsom: The semi-arid mountain valley of the Central Himalaya. Atmos. Res. 234, 104691, https://doi.org/10.1016/j.atmosres.2019.104691, 2020.

Wang, L., Wang, S., Zhang, L., Wang, Y., Zhang, Y., Nielsen, C., McElroy, M.B., Hao, J.: Source apportionment of atmospheric mercury pollution in China using the GEOS-Chem model. Environ. Pollut. 190, 166-175, https://doi.org/10.1016/j.envpol.2014.03.011, 2014.

https://doi.org/10.5194/essd-2025-551
Preprint. Discussion started: 13 March 2026

Wang, J., Sun X., Li M., Li S., Guo J., Zhang Q.: Seasonal Variation and relationship between mercury and suspended particulate matter in Hailuogou glacier meltwater runoff. Earth and Environment, 50, 320-327. In Chinese with English abstract, 2022.

Wang, J., Guo, J., Sun, X., Li, M., Liu, Y., Lu, Z., Kang, S., and Zhang, Q.: Co-analysis of total suspended particles and discharge reveals the dynamic of mercury input into glacier meltwater runoff in the northern Tibetan Plateau. Sci. Total Environ. 954, 176458, https://doi.org/10.1016/j.scitotenv.2024.176458, 2024.

Yang, Z., Guo, J., Sun, S., Ni, D., Chen, P., Rupakheti, D., Kang, H., Abdullaev, S.F., Abdyzhapar uulu, S., and Kang, S.: Spatial distribution and risk assessments of mercury in topsoils of Central Asia. Geosci. Front. 14, 101585, https://doi.org/10.1016/j.gsf.2023.101585, 2023.

Yang, M., Nelson, F. E., Shiklomanov, N. I., Guo, D., and Wan, G.: Permafrost degradation and its environmental effects on the Tibetan Plateau: A review of recent research. Earth-Sci. Rev. 103(1-2), 31-44, http://dx.doi.org/10.1016/j.earscirev.2010.07.002, 2010.

Yin, R., Krabbenhoft, D.P., Bergquist, B.A., Zheng, W., Lepak, R.F., and Hurley, J.P.: Effects of mercury and thallium concentrations on high precision determination of mercury isotopic composition by Neptune Plus multiple collector inductively coupled plasma mass spectrometry. J. Anal. Atom. Spectrom. 31, 2060-2068, https://doi.org/10.1039/C6JA00107F, 2016a.

Yin, R., Feng, X., Hurley, J.P., Krabbenhoft, D.P., Lepak, R.F., Kang, S., Yang, H., and Li, X.: Historical records of mercury stable isotopes in sediments of Tibetan lakes. Sci. Rep. 23332, https://doi.org/10.1038/srep23332, 2016b.

Yao, T., Masson-Delmotte, V., Gao, J., Yu, W., Yang, X., Risi, C., Sturm, C., Werner, M., Zhao, H., He, Y., Ren, W., Tian, L., Shi, C., and Hou, S.: A review of climatic controls on $\delta^{18}O$ in precipitation over the Tibetan Plateau: Observations and simulations. Rev. Geophys. 51, 525-548, https://doi.org/10.1002/rog.20023, 2013.

Yao, T., Xue, Y., Chen, D., Chen, F., Thompson, L., Cui, P., Koike, T., Lau, W.K.-M., Lettenmaier, D., Mosbrugger, V., Zhang, R., Xu, B., Dozier, J., Gillespie, T., Gu, Y., Kang, S., Piao, S., Sugimoto, S., Ueno, K., Wang, L., Wang, W., Zhang, F., Sheng, Y., Guo, W., Ailikun, Yang, X., Ma, Y., Shen, S.S.P., Su, Z., Chen, F., Liang, S., Liu, Y., Singh, V.P., Yang, K., Yang, D., Zhao, X., Qian, Y., Zhang, Y., and Li, Q.: Recent Third Pole's rapid warming accompanies cryospheric melt and water cycle intensification and interactions between monsoon and environment: Multidisciplinary approach with observations, modeling, and analysis. Bull. Amer. Meteorol. Soc. 100, 423-444, https://doi.org/10.1175/BAMS-D-17-0057.1, 2019.

Yao, T., Bolch, T., Chen, D., Gao, J., Immerzeel, W., Piao, S., Su, F., Thompson, L., Wada, Y., Wang, L., Wang, T., Wu, G., Xu, B., Yang, W., Zhang, G., and Zhao, P.: The imbalance of the Asian water tower. Nat. Rev. Earth Environ. 3, 618-632, https://doi.org/10.1038/s43017-022-00299-4, 2022.

Yin, X., Kang, S., de Foy, B., Ma, Y., Tong, Y., Zhang, W., Wang, X., Zhang, G., and Zhang, Q.: Multi-year monitoring of atmospheric total gaseous mercury at a remote high-altitude site (Nam Co, 4730 m a.s.l.) in the inland Tibetan Plateau region, Atmos. Chem. Phys., 18, 10557–10574, https://doi.org/10.5194/acp-18-10557-2018, 2018.

Yin, X., Zhou, W., Su, Y., Tang, C., Guo, J., Liu, Z., Wang, Y., Zhang, X., Rupakheti, D., and Kang, S.: Spatial distribution and risk assessment of mercury in soils over the Tibetan Plateau. Sci. Total Environ. 954, 176652, https://doi.org/10.1016/j.scitotenv.2024.176652, 2024.

You, Q., Cai, Z., Pepin, N., Chen, D., Ahrens, B., Jiang, Z., Wu, F., Kang, S., Zhang, R., Wu, T., Wang, P., Li, M., Zuo, Z., Gao, Y., Zhai, P., and Zhang, Y.: Warming amplification over the Arctic Pole and Third Pole: Trends, mechanisms and consequences. Earth Sci. Rev. 217, 103625, https://doi.org/10.1016/j.earscirev.2021.103625, 2021.

https://doi.org/10.5194/essd-2025-551
Preprint. Discussion started: 13 March 2026

1026 Zhang, Q., Huang, J., Wang, F., Loewen, M., Xu, J., Armstrong, D., Li, C., Zhang, Y., and Kang, S.: Mercury distribution
1027 and deposition in glacier snow over western China. Environ. Sci. Technol. 46, 5404-5413,
1028 https://doi.org/10.1021/es300166x, 2012.
1029 Zheng, W., Kang, S.C., Feng, X.B., Zhang, Q.G., and Li, C.L.: Mercury speciation and spatial distribution in surface waters
1030 of the Yarlung Zangbo River, Tibet. Chin. Sci. Bull. 55, 2697-2703, https://doi.org/10.1007/s11434-010-4001-y,
1031 2010.
1032 Zhang, Y., Jacob, D.J., Horowitz, H.M., Chen, L., Amos, H.M., Krabbenhoft, D.P., Slemr, F., St. Louis, V.L., and
1033 Sunderland, E.M.: Observed decrease in atmospheric mercury explained by global decline in anthropogenic
1034 emissions. Proc. Nat. Acad. Sci. 113, 526, https://doi.org/10.1073/pnas.1516312113, 2016.